

**NOVEL ELECTROCHEMICAL CAPACITORS BASED ON
FREE-STANDING SINGLE-WALLED CARBON NANOTUBE FILMS**

by

Xin Li

A thesis submitted to the Faculty of the University of Delaware in partial fulfillment of the requirements for the degree of Master of Science in Mechanical Engineering

Spring 2012

© 2012 Xin Li
All Rights Reserved

**NOVEL ELECTROCHEMICAL CAPACITORS BASED ON
FREE-STANDING SINGLE-WALLED CARBON NANOTUBE FILMS**

by

Xin Li

Approved: _____
Bingqing Wei, Ph.D.
Professor in charge of thesis on behalf of the Advisory Committee

Approved: _____
Anette M. Karlsson, Ph.D.
Chair of the Department of Mechanical Engineering

Approved: _____
Babatunde A. Ogunnaike, Ph.D.
Dean of the College of Engineering

Approved: _____
Charles G. Riordan, Ph.D.
Vice Provost for Graduate and Professional Education

ACKNOWLEDGMENTS

It has been an unforgettable experience for me to study and execute research in the University of Delaware in the past two and half years. I received much support from the faculty, staff, colleagues, family and friends here.

I would like to firstly convey my deepest thankfulness to my mentor and advisor, Dr. Bingqing Wei. I am proud to be one of his students, and passionate about the mission, vision and values of our group. Dr. Wei encourages us to be self-motivated and driven to perform at our highest potential. Dr. Wei requires us to always contribute new ideas, think innovatively, and do the significant research that no groups ever did. Dr. Wei's diligence, pursuit of excellence and optimistic image set me a role model for me to learn through the rest of my life, and remind me to always "go the extra mile".

I wish to thank Dr. Chaoying Ni, Dr. Ajay Prasad, and Dr. Joshua Hertz for accepting my request to join my thesis committee, and for the teaching and discussion throughout my study here. Specifically, I want to thank Dr. Ni for the teaching on the SEM and TEM instruments.

I hope to thank Dr. Jonghwan Suhr, who in the final semester provided me financial support and the challenging work for me to explore. Also, I hope to thank Dr. Lian-ping Wang, and Dr. Tsu-Wei Chou for discussions and encouragements. I wish to express gratitude to Mrs. Lisa Katzmire, Letitia Toto, Elizabeth Bonavita, and Roger Stahl, who provided valuable support.

I would like to acknowledge my former colleague, Jiepeng Rong and Dr. Jinhai Liu, who taught me hand by hand those important skills when I joined Dr. Wei's group from January to June, 2010. I would also like to thank my current colleagues, Qing Zhang, Zeyuan Cao, Jinwen Qin, Stephen Mulligan, Chuan Cai, Taoli Gu, Dr. Jianxiong Liu, for all the important discussions toward understanding and improvement.

Nothing can be done brilliantly without loving and supportive parents. I would love to convey my true gratefulness to my mother, Mrs. Jinying An, and my father, Mr. Jiansen Li, for your unconditional love and your support throughout my life.

Last but not least, I would love to thank my dear wife, Zhen Wang. You grant me the pride, the passion, and the enthusiasm toward our common goal to cultivate the harmonious family with peace and love, through the full engagement both in career and at home. Thank you for the every single moment that we spend together, your patience, support and love.

DEDICATION

To the loving memory of my grandfather,
Qide Li,
a man who fight until the very end of his life.

To my mother, Jinying An,
my father, Jiansen Li,
and my wife, Zhen Wang,
who make all our efforts meaningful,
and our life colorful.

TABLE OF CONTENTS

LIST OF TABLES	ix
LIST OF FIGURES	x
ABSTRACT	xiii

Chapter

1	INTRODUCTION	1
1.1	Introduction to Supercapacitors	1
1.2	Charge and Discharge Mechanism of the Double Layer Capacitor	4
1.3	Redox Reaction Based Supercapacitor	6
	REFERENCES	8
2	ELECTROCHEMICAL BEHAVIOR OF SINGLE-WALLED CARBON NANOTUBE SUPERCAPACITORS UNDER COMPRESSIVE STRESS	12
2.1	Significance	12
2.2	Literature Review of the Flexible Supercapacitor	12
2.3	Experimental Section	13
2.3.1	Fabrication of the SWNT Macro-film Electrodes	13
2.3.2	Flexible Supercapacitor Assembly	15
2.3.3	Electrochemical Measurements	17
2.3.4	Contact Angle Measurements	17
2.4	Results and Discussion	18
2.4.1	Pressure Effect on the Specific Capacitance	18
2.4.2	Ion Size Effect and Surface Wettability Effect for Different Electrolyte	21
2.4.3	Electrochemical Impedance Spectroscopy Study	24
2.5	Conclusions	35

	REFERENCES.....	37
3	DYNAMIC STRETCHABLE SUPERCAPACITOR BASED ON BUCKLED SINGLE-WALLED CARBON NANOTUBE MACROFILMS AND ELASTOMERIC SEPARATOR.....	40
3.1	Significance	40
3.2	Literature Review of Stretchable Electronics and Stretchable Energy Storage Devices	41
3.3	Experimental Section.....	43
3.3.1	Compliant Polydimethylsiloxane Substrate Fabrication	43
3.3.2	Electrospinning of Polyurethane Elastomeric Separator.....	43
3.3.3	Dynamically Stretchable Supercapacitor Assembly	44
3.3.4	Electrochemical Characterization.....	45
3.3.5	Morphology Characterization.....	45
3.4	Results and Discussion	46
3.4.1	Concept and Morphology of the Components.....	46
3.4.2	Electrochemical Behavior of DSS at static 0% Strain and 31.5% Strain.....	48
3.4.3	Electrochemical Behavior of the DSS under DSR Mode.....	51
3.5	Conclusion.....	60
	REFERENCES.....	62
4	FACILE SYNTHESIS AND SUPER CAPACITIVE BEHAVIOR OF SINGLE-WALLED CARBON NANOTUBE AND MANGANESE OXIDE HYBRID FILMS.....	65
4.1	Significance	65
4.2	Literature Review of Pseudocapacitive Materials	66
4.3	Introduction to SWNT/MnO ₂ Hybrid Film	66
4.4	Experimental Section.....	68
4.4.1	Preparation of SWNT/MnO ₂ Hybrid Films Electrodes	68

4.4.2	Structural Characterization and MnO ₂ Loading Measurement	68
4.4.3	Electrochemical Measurements	69
4.5	Results and Discussion	70
4.5.1	Reaction Mechanism to Synthesize SWNT/MnO ₂ Hybrid Films	70
4.5.2	Electrochemical Behavior of the SWNT/MnO ₂ Hybrid Films	73
4.6	Conclusions	87
	REFERENCES	89
5	CONCLUSIONS, PUBLICATIONS AND FUTURE WORK	93
5.1	Conclusions	93
5.2	Publications	94
5.3	Future Work	95

LIST OF TABLES

Table 2.1	Contact Angle of Different 1 M Electrolyte on the Surface of SWNT Electrode.....	21
Table 2.2	Slope (g) of the surface tension equation	22
Table 2.3	Pauling ionic radii (r_p), hydrated ion size ($2d_{ion}$), Capacitance under 1723.96 kPa	23
Table 2.4	Knee frequency (experiment data) vs. Pressure	30
Table 3.1	AC impedance equivalent circuit fitting parameters in ZVIEW.....	58
Table 4.1	Impedance curve fitting results of the SWNT/MnO ₂ and the SWNT electrodes, before and after long cycling, in TEABF ₄ /PC using ZVIEW.	85

LIST OF FIGURES

Figure 1.1	Ragone plot of various electrochemical energy storage devices. Time constants are shown in dashed line, by dividing the specific energy by the specific power. The shaded curves were obtained from ref [5].	2
Figure 1.2	Schematic of charged and discharged states of an electric double layer capacitor.	4
Figure 2.1	SEM of SWNT macro-film after heat and acid treatment.	15
Figure 2.2	(a) Schematic of supercapacitor assembly with SWNT electrodes. (b) Digital camera image of assembled flexible supercapacitor. (c) Schematic of pressure applied facility on supercapacitor.....	16
Figure 2.3	Specific capacitance increase trend under pressure effect for electrolytes. (a) LiOH, NaOH, KOH. (b) LiCl, NaCl, KCl, and KNO ₃	19
Figure 2.4	Cyclic voltammetry at 50 mV s ⁻¹ of the SWNT supercapacitors with 1 M electrolyte under increasing applied pressure (kPa). (a) LiOH (b) LiCl (c) NaOH (d) NaCl (e) KOH (f) KCl (g) KNO ₃	20
Figure 2.5	Impedance results with "knee" frequency of the SWNT supercapacitors under small applied pressures (a) LiOH (b) LiCl (c) NaOH (d) NaCl (e) KOH (f) KCl (g) KNO ₃	26
Figure 2.6	Impedance results with "knee" frequency of the SWNT supercapacitors under large applied pressures. (a) LiOH (b) LiCl(c) NaOH (d) NaCl (e) KOH (f) KCl(g) KNO ₃	27
Figure 2.7	Impedance curve fitting results for each element in equivalent circuit (a) AC impedance equivalent circuit. (b) Series Resistance, (c) Charge transfer resistance, (d) Warburg diffusion resistance, (e) Warburg time constant, and (f) Double layer capacitance.	28

Figure 2.8	Schematic representation of the cations/anions in aqueous electrolyte/SWNT electrode interface during the pressure increase process with Helmholtz planes presented by the semitransparent orange band. (a) LiOH under small pressure, (b) LiCl under small pressure, (c) LiOH under large pressure, and (d) LiCl under large pressure.....	33
Figure 3.1	a) Schematic of the main components of the DSS. b) Schematic of the DSS under 0% strain and 31.5% strain.	47
Figure 3.2	a) SEM image of the electrospun elastomeric separator. b) Optical image of the buckled SWNT film	47
Figure 3.3	CV curves of DSS under static 0 % strain and 31.5 % strain at a) 2000 mV s^{-1} scan rate. b) 50 mV s^{-1} scan rate. c) summary of the specific capacitance vs. scan rates (from 50 mV s^{-1} to 2000 mV s^{-1}).....	50
Figure 3.4	CV curves of DSS a) under fixed 0 % strain and 31.5 % strain. b) schematic of CV curve under DSR mode: gradually changes between CV curve at fixed 31.5% strain and fixed 0% strain. c) CV curves under dynamic stretching releasing (DSR) at 2.22% strain rate s^{-1} d) at 4.46% strain rate s^{-1} (Scan rate is 100 mV s^{-1} .).....	53
Figure 3.5	a) Galvanostatic charge/discharge curve at current density of 10 A g^{-1} , during <i>In situ</i> DSR at strain rate of 4.46 % strain s^{-1} b) Comparison of the normalized capacitance (the capacitance divided by the initial capacitance value of the DSS fixed at static 31.5 % strain) with different strain rate. c) Enlarged figure to compare the specific capacitance of the cell under different strain rate applied. d) With <i>In situ</i> applied DSR cycling at high strain rate of 1.11 % s^{-1} strain s^{-1} , and 4.46 % strain s^{-1} , the DSS shows good cycling stability. The current density is 10 A g^{-1}	56
Figure 3.6	a) Nyquist plots of DSS at different strain and strain rate applied and the equivalent circuit in ZVIEW software (inset: high frequency region) b) Schematic of the DSS at different strain applied showing changing electrode/electrolyte interface due to stretching/releasing.....	57
Figure 4.1	Schematic illustration of the synthesis process of nano- MnO_2 on the surface of SWNTs macro-film and the corresponding snapshots of the process taken with a camera.	70

Figure 4.2	SEM images of a) SWNT film as synthesized before coating MnO ₂ layer. b) SWNT/MnO ₂ electrode material as-synthesized. c) SWNT/MnO ₂ electrode material after 15,000 th cycles.....	72
Figure 4.3	a) CV curves of SWNT/MnO ₂ electrode measured at different scan rates (50 mV s ⁻¹ to 2,000 mV s ⁻¹). b) Comparative CV curves of SWNT/MnO ₂ and SWNT at scan rate of 500 mV s ⁻¹ . c) TEM image of SWNT/MnO ₂ electrode material before cycling. d) TEM image of SWNT/MnO ₂ electrode material after the 15,000 th cycles cycling.	75
Figure 4.4	a) Comparison of specific capacitances of SWNT/MnO ₂ electrode (blue line: based on mass of MnO ₂ ; red line: based on total mass of SWNT/MnO ₂) and SWNT electrode at different scan rates. b) Ragone plots of SWNT/MnO ₂ electrode and SWNT electrode at different current densities (0.1 A g ⁻¹ to 100 A g ⁻¹). Green and orange transparent regions indicate the Ragone plot of Ni-MH and Li-ion batteries extracted from ref. [28]. c) Galvanostatic charge/discharge curves of SWNT/MnO ₂ at different current densities (5 A g ⁻¹ to 100 A g ⁻¹).....	80
Figure 4.5	Cycle performance comparison of SWNT/MnO ₂ electrode and SWNT electrode in TEABF ₄ /PC electrolyte. a) 15,000 cycles at current density of 50 A g ⁻¹ . b) 1,000 cycles at current density of 2 A g ⁻¹ . c) Randomly-picked continuous 6 charge-discharge cycle profile of SWNT/MnO ₂ electrode at current density of 2 A g ⁻¹ . d) Galvanostatic charge/discharge curves from the 1 st to the 1,000 th cycles for SWNT/MnO ₂ and SWNT electrode at 2 A g ⁻¹ (arrow indicates the direction where cycle number is increasing).	82
Figure 4.6	Nyquist plots of a) SWNT/MnO ₂ and b) SWNT electrode before and after 1,000 cycles with the electrical equivalent circuits used for fitting impedance spectra.	84

ABSTRACT

In order to effectively store the energy from the renewable sources and release them when needed, energy storage devices play an important role. Among all the energy storage devices, the electrochemical capacitor currently holds the highest power density and modest energy density. Nanostructured materials have shown promising electrochemical performance as electrode materials for electrochemical capacitor and different carbon nanostructured materials are under close scrutiny. Among those, carbon nanotube films draw great attention owing to their extraordinary properties, such as high surface area, excellent electrical conductivity, and mechanical robustness.

In this thesis, the electrochemical capacitors based on freestanding single-walled carbon nanotube (SWNT) film are investigated from three perspectives.

First, the effect of compressive stress on the electrochemical behavior of flexible supercapacitors based on the freestanding SWNT film electrodes and 1 M aqueous electrolytes with different anions and cations were investigated. The results demonstrated that the specific capacitance increased firstly and saturated in corresponding to decreases of the series resistance, the charge transfer resistance, and the Warburg diffusion resistance under an increased pressure from 0 to 1723.96 kPa. The wettability and the ion-size effect play important roles to determine the pressure

dependence behavior of the supercapacitors. An improved high frequency capacitive response with 1172 Hz "knee" frequency was observed under the compressive pressure of 1723.96 kPa.

Second, a dynamically stretchable supercapacitor (DSS) with highly reversible stretchability was demonstrated based on the elastomeric electrospun polyurethane separator, the buckled SWNT macrofilms electrodes, and organic electrolyte. The electrochemical behavior of the stretchable cells was instantaneously characterized under both dynamic stretch/release (DSR) and fixed static strain modes. The interesting capacitance variation was observed under the DSR mode, which corresponds with the state of the strain and strain rate applied. The capacitance variation is mainly attributed to the changes of charge transfer resistance and Warburg diffusion resistance during the stretching/releasing. The cells have shown excellent cycling stabilities under cyclic stretching/releasing.

Third, the SWNT/MnO₂ hybrid films as supercapacitor electrode materials were synthesized using a new and facile approach, which is binder-free, robust and with pre-formed electrical pathways. The one-step precipitation process is facile, cost-effective and scalable for mass production of the electrode materials with enhanced electrochemical performances. The supercapacitors demonstrate a much improved energy density and equally high power density, as well as an ultra-high frequency response and excellent long-cycle stability. The energy density of 70 Wh kg⁻¹ with power density of 77.3 W kg⁻¹ shows its high competitiveness compared with the

current Ni-MH battery systems, thus makes the supercapacitors very promising to be implemented as the electric energy storage devices for hybrid vehicles.

Chapter 1

INTRODUCTION

1.1 Introduction to Supercapacitors

In the recent decades, global warming and largely deprived non-renewable resource have urged the society to shift from a fossil fuel based economy to a more sustainable and environmentally-friendly system. With the exponentially growing portion of electricity generated from renewable resources (solar, wind, and tidal power) in total electricity production throughout the globe, the mission of implementing the environmentally-friendly energy storage technologies is even more vital to the future of global sustainable economy. Moreover, energy storage technology to ensure high quality power supply is not only important for developed countries in terrestrial application, but also critical for the two billion people who live in the area which lack of traditional power grid infrastructure, and for space probes or unmanned ocean vehicles to carry out scientific research and exploration.

As shown in Fig. 1.1, Ragone plot[1] is illustrated in order to compare the performance of various energy storage devices, including symmetric supercapacitors [2], hybrid (asymmetric) supercapacitors [3] , and Li-ion batteries [4].

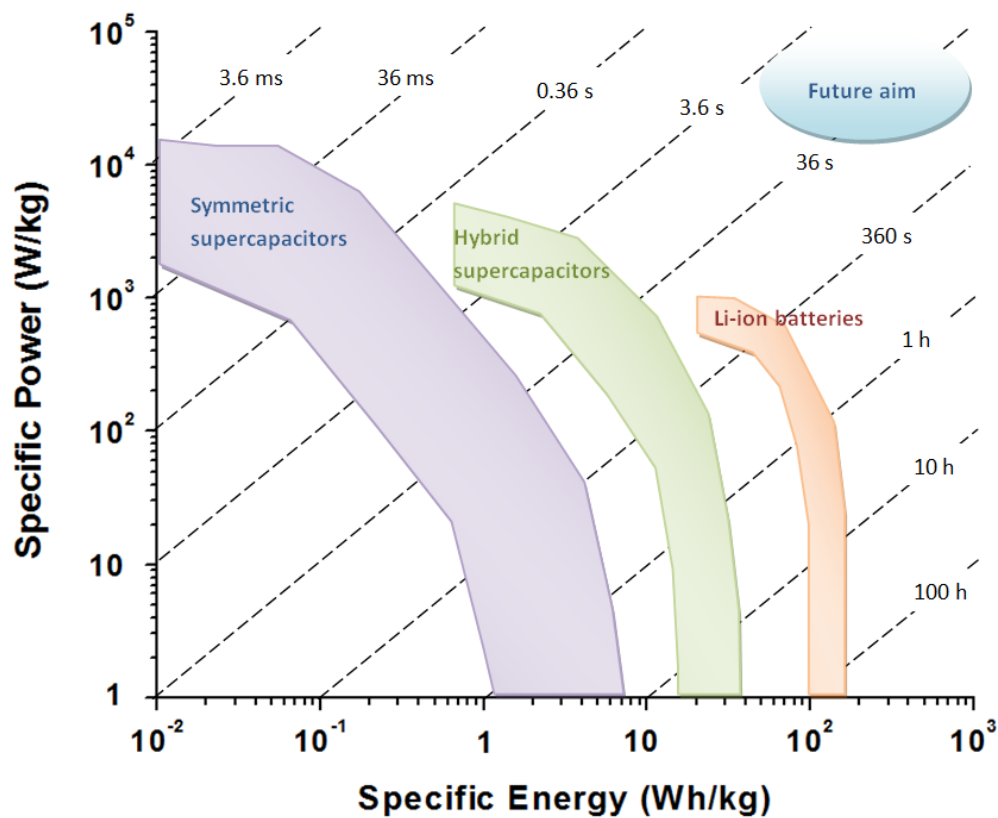


Figure 1.1 Ragone plot of various electrochemical energy storage devices. Time constants are shown in dashed line, by dividing the specific energy by the specific power. The shaded curves were obtained from ref [5].

Among the current three major energy storage devices, the typical symmetric supercapacitor have much higher power density from 5 to 55 kW kg⁻¹, and can be fully charged or discharged in less than 1 s because of the rapid movement of ions in the electrolyte to form the electrical double layer. Additionally, the symmetric supercapacitor exhibits extremely high electrochemical cycling stability, compared to the Li-ion batteries. In between the Li-ion batteries and symmetric supercapacitors, the newly developed hybrid (asymmetric) supercapacitor, which combines a redox

electrode with an electric double layer electrode, providing energy density from 10 to 50 Wh kg⁻¹, and power density from 1 to 5 kW kg⁻¹[6], complementing the energy and power gap between the symmetric supercapacitors and the Li-ion batteries.

For all the available electrode materials, nanostructure carbon-based materials have been widely researched and utilized for supercapacitors, because of their high electrical conductivity, high specific surface area (from 1000 m² g⁻¹ to 2600 m² g⁻¹), excellent corrosion resistance, high temperature stability, tunable pore structure, and relatively low cost[7]. To date, different form of carbon materials, such as activated carbons(ACs)[8], templated carbons[9], carbide-derived carbons(CDCs)[10], activated carbon fabrics[11], carbon fibers[12], carbon aerogels[13], carbon nanotubes(CNTs)[14], carbon nanohorns[15], and carbon onions [16] have been utilized both for symmetric and asymmetric supercapacitors. Most recently, graphene [17-19] and graphene composite [20] have also been investigated because of their unique structures and high specific surface areas (2630 m² g⁻¹ for graphene).

1.2 Charge and Discharge Mechanism of the Double Layer Capacitor

Depending on the charge/discharge mechanism, inherently most of the high surface area, carbon-based supercapacitor works as electrical double layer capacitors (EDLCs). As shown in Fig. 1.2, EDLCs store energy by electrostatic charge accumulation at electrode/electrolyte interfaces. Because of this feature, they have better cycling performance and power density than the hybrid supercapacitors and Li-ion batteries. During charge phase, the surface of the electrodes attracts the ions of opposite charge in the electrolyte, which form the electrical double layers (EDLs).

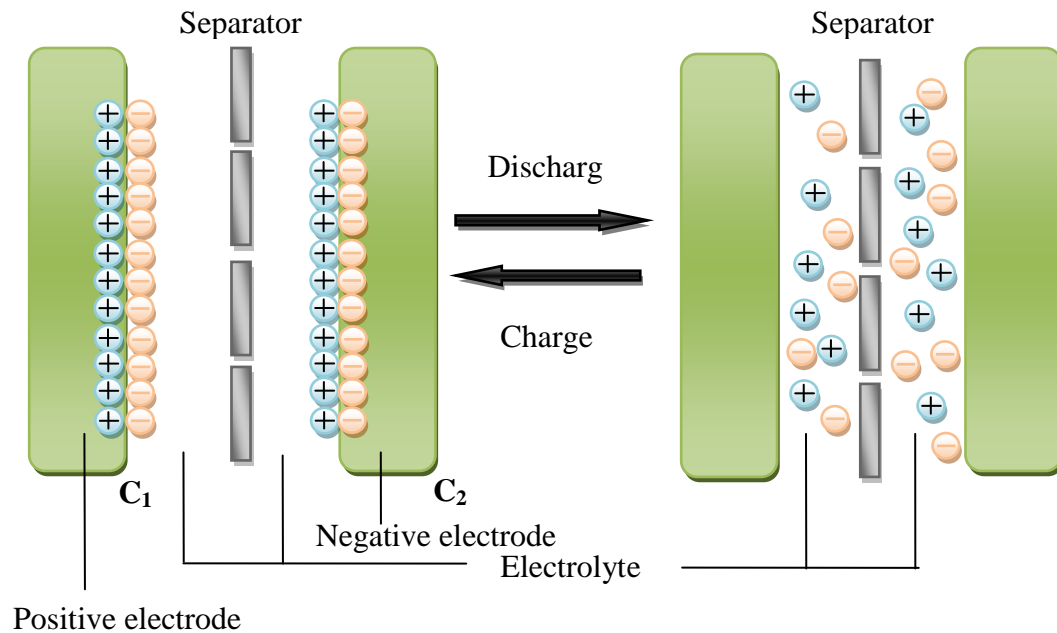


Figure 1.2 Schematic of charged and discharged states of an electric double layer capacitor.

Each electrode (C_1) or (C_2) is equivalent to a capacitor with capacity given by:

$$C_{dl} = \frac{\varepsilon S}{d} \quad (1.1)$$

where S is the surface area of the electrode/electrolyte interface, ε is the permittivity of dielectric constant, d is the effective thickness of the electrical double layer.

The total capacitance can be calculated and is more affected by the electrode with the smallest capacitance according to:

$$\frac{1}{C} = \frac{1}{C_1} + \frac{1}{C_2} \quad (1.2)$$

The energy (E) of a supercapacitor is calculated as:

$$E = \frac{1}{2} C U^2 \quad (1.3)$$

where C is the capacitance in Farads, and U is the operating voltage of the capacitor, which depends on the electrolyte stability window (ESW).

The power (P) of supercapacitor is calculated as:

$$P = \frac{U^2}{4R_s} \quad (1.4)$$

where R_s is the equivalent series resistance (ESR) of the supercapacitor. The ESR of supercapacitor is contributed by: (i) intrinsic electronic resistance of the electrode, (ii) the resistance between the electrode and the current collector, (iii) the electrolyte resistance, (iv) the charge transfer resistance at the electrode/electrolyte interface, (iv) the ionic resistance of ions moving through the separator. [21]

According to the Equation (1.3) and (1.4), theoretically the larger ESW provided by the electrolyte, the higher energy density and power density a

supercapacitor can achieve. Currently, there are three main groups of liquid electrolyte: (i) aqueous electrolyte, (ii) conventional organic electrolyte, (iii) ionic liquids (ILs) electrolyte.

For symmetric capacitors, the voltage window for aqueous electrolyte is typically limited to 1 V (due to the thermodynamic decomposition of water). However recently, this limited voltage for symmetric EDLCs has been improved to 1.6 V using neutral Na_2SO_4 electrolyte, achieved with AC electrode and graphene electrode[22,23,24]. The conventional organic electrolyte typically using tetraethylammonium tetrafluoroborate (TEABF_4) salts, allowing the cell operating voltage to be around 2.3V[25]. Comparatively, ILs electrolyte currently provide the widest ESW, ranging from 4 to 6 V[26,27,28]. The most widely used hydrophobic ILs are N-butyl-N-methylpyrrolidinium-bis(trifluoromethanesulfonyl)imide ($\text{PYR}_{14}\text{TFSI}$)[29] and 1-ethyl-3-methyl-imidazolium-bis(trifluoromethanesulfonyl)imide (EMITFSI)[30].

1.3 Redox Reaction Based Supercapacitor

Redox capacitance (Pseudocapacitance) at the electrode/electrolyte interface is different than the double layer charge storage mechanism. Compared to the electrostatic capacitance of double layer capacitor, the redox capacitor is intrinsically Faradaic, involving the passage of charge across the double layer, similar to the charging mechanism of batteries[31]. The redox reactions usually take place at the top

thin layer of the electrode surface. Thus, the energy density of the redox reaction is usually higher than the pure EDL capacitor. Typically, the redox materials can be divided by two groups: (i) conductive polymers (CPs) [32, 33], (ii) transition metal oxides (TMOs) [34].

Although the redox materials typically provide higher capacitance and energy density, due to the reversible redox reaction in the near-surface regions, however most of the materials do not have good electrical conductivity. Thus, they are often combined with nanostructured carbon materials to increase the power performance [35, 36] and cycling stability.

REFERENCES

- [1] R. F. Service, "*New 'supercapacitor' promises to pack more electrical punch*" Science, vol. 313, pp. 902-905, 2006.
- [2] K. S. Ryu, K. M. Kim, N. G. Park, S. H. Chang, "*Symmetric redox supercapacitor with conducting polyaniline electrode*" Journal of Power Sources, vol. 103, pp.305-309, 2002.
- [3] A. D. Pasquier, I. Plitz, J. Gural, S. Menocal, G. Amatucci, "*Characteristics and performance of 500 F asymmetric hybrid advanced supercapacitor prototypes*" Journal of Power Sources, vol. 113 pp.62-71, 2003.
- [4] J.-M. Tarascon, M. Armand, "*Issues and challenges facing rechargeable lithium batteries*" Nature, vol. 414, pp. 359–367, 2001.
- [5] P. Simon, Y. Gogotsi, "*Materials for electrochemical capacitors*", Nature Materials, vol. 7, pp. 845-854, 2008.
- [6] X. Zhao, C. Johnston, P.S. Grant, "*A novel hybrid supercapacitor with a carbon nanotube cathode and an iron oxide/carbon nanotube composite anode*", Journal of Materials Chemistry, vol. 19, pp.8755-8760, 2009.
- [7] A.G. Pandolfo, A.F. Hollenkamp. "*Carbon properties and their role in supercapacitors*", Journal of Power Sources, vol. 157, pp.11-27, 2006.
- [8] J. Gamby, P. L. Taberna, P. Simon, J. F. Fauvarque, M. Chesneau, "*Studies and characterisations of various activated carbons used for carbon/carbon supercapacitors*", Journal of Power Sources, vol. 101, pp.109-116, 2001.
- [9] A.B. Fuertes, G. Lota, T.A Centeno, E. Frackowiak, "*Templated mesoporous carbons for supercapacitor application*" Electrochimica Acta, vol. 50, pp. 2799-2805, 2005.
- [10] J. Chmiola, G. Yushin, R. Dash, Y. Gogotsi, "*Effect of pore size and surface area of carbide derived carbons on specific capacitance*" Journal of Power Sources, vol. 158, pp.765-772, 2006.

- [11] K. Babel, K. Jurewicz, "*KOH activated carbon fabrics as supercapacitor material*" *Journal of Physics and Chemistry of Solids*, vol. 65, pp.275-280, 2005.
- [12] C. Merino, P. Soto, E. V. Ortego, J. M. Gomez de Salazar, F. Pico, J. M. Rojo, "*Carbon nanofibres and activated carbon nanofibres as electrodes in supercapacitors*" *Carbon*, vol. 43, pp. 551-557, 2005.
- [13] H. Probstle, M. Wiener, J. Fricke, "*Carbon Aerogels for Electrochemical Double Layer Capacitors*" *Journal of Porous Materials*, vol. 10, pp.213–222, 2003.
- [14] D. N. Futaba, K. Hata, T. Yamada, T. Hiraoka, Y. Hayamizu, Y. Kakudate, O. Tanaike, H. Hatori, M. Yumura, S. Iijima, "*Shape-engineerable and highly densely packed single-walled carbon nanotubes and their application as super-capacitor electrodes*" *Nature Materials*, vol. 5, pp.987-994, 2006.
- [15] C.M. Yang, Y.J. Kim, M. Endo, H. Kanoh, M. Yudasaka, S.Iijima, K.Kaneko, "*Nanowindow-regulated specific capacitance of supercapacitor electrodes of single-wall carbon nanohorns*" *Journal of the American Chemical Society*, vol. 129, pp.20-21, 2007.
- [16] E.G.Bushueva, P.S.Galkin, A.V. Okotrub, L.G.Bulusheva, N.N. Gavrilov, V. L. Kuznetsov, S. I. Moiseev, "*Double layer supercapacitor properties of onion-like carbon materials*" *Physica Status Solidi (B) Basic Research*, vol. 245, pp. 2296–2299, 2008.
- [17] Y. Wang, Z. Shi, Y. Huang, Y. Ma, C. Wang, M. Chen, Y. Chen, "*Supercapacitor devices based on graphene materials*" *The Journal of Physical Chemistry C*, vol. 113, pp.13103–13107, 2009.
- [18] M. D. Stoller, S. Park, Y. Zhu, J. An, R. S. Ruoff, "*Graphene-based ultracapacitors*" *Nano Letters*, vol. 8, pp. 3498-3502, 2008.
- [19] Y. Zhu, S. Murali, M. D. Stoller, K.J. Ganesh, W. Cai, P.J. Ferreira, A. Pirkle, R.M. Wallace, K.A. Cychosz, M. Thommes, D. Su, E.A. Stach, R. S. Ruoff, "*Carbon-based supercapacitors produced by activation of graphene*" *Science*, vol. 332, pp.1537-1541, 2011.
- [20] D.W. Wang, F. Li, J. Zhao, W. Ren, Z. Chen, J. Tan, Z. S. Wu, I. Gentle, G. Q. Lu, H. M. Cheng, "*Fabrication of graphene/polyaniline composite paper via in situ*

anodic electropolymerization for high-performance flexible electrode" ACS Nano, vol. 3, pp.1745-1752, 2009.

[21] T. Osaka, M. Datta, *Energy Storage Systems in Electronics (New Trends in Electrochemical Technology)*, CRC press, 1st edition, 2000.

[22] L. Demarconnay, E. Raymundo-Pinero, F. Beguin, "A symmetric carbon/carbon supercapacitor operating at 1.6V by using a neutral aqueous solution" *Electrochemistry Communications*, vol. 12, pp. 1275-1278, 2010.

[23] M.P. Bichat, E. Raymundo-Pinero, F. Beguin, "High voltage supercapacitor built with seaweed carbons in neutral aqueous electrolyte" *Carbon*, vol. 48, pp. 4351-4361, 2010.

[24] X. Yang, Y. He, G. Jiang, X. Liao, Z. Ma, "High voltage supercapacitors using hydrated graphene film in a neutral aqueous electrolyte" *Electrochemistry Communications*, vol. 13, pp 1166-1169, 2011.

[25] E. Frackowiak, "Carbon materials for supercapacitor application" *Physical Chemistry Chemical Physics*, vol. 9, pp.1774-1785, 2007.

[26] M.C. Buzzeo, R.G. Evans, R.G. Compton, "Non-haloaluminate room-temperature ionic liquids in electrochemistry-A review" *A European Journal Chem Phys Chem*, vol. 5, pp. 1106-1120, 2004.

[27] C. Arbizzani, M. Bisio, D. Cericola, M. Lazzari, F. Soavi, M. Mastragostino, "Safe, high-energy supercapacitors based on solvent-free ionic liquid electrolytes" *Journal of Power Sources*, vol. 185, pp. 1575–1579, 2008.

[28] C. Arbizzani, S. Beninati, M. Lazzari, F. Soavi, M. Mastragostino, "Electrode materials for ionic liquid-based supercapacitors" *Journal of Power Sources*, vol.174 pp.648–652, 2007.

[29] A. Balducci, R. Dugas, P.L. Taberna, P. Simon, D. Plee, M. Mastragostino, S. Passerini, "High temperature carbon-carbon supercapacitor using ionic liquid as electrolyte" *Journal of Power Sources*, vol. 165, pp. 922–927, 2007.

[30] M. Lazzari, M. Mastragostino, F. Soavi, "Capacitance response of carbons in solvent-free ionic liquid electrolytes" *Electrochemistry communications*, vol. 9, pp. 1567–1572, 2007.

- [31] B.E. Conway, "*Electrochemical supercapacitors: scientific fundamentals and technological applications*", Kluwer Academic and Plenum, New York, 1999.
- [32] K. S. Ryu, K. M. Kim, N. G. Park, Y. J. Park, S. H. Chang, "*Symmetric redox supercapacitor with conducting polyaniline electrodes*" *Journal of Power Sources*, vol.103, pp. 305-309, 2002.
- [33] J. H. Park, J. M. Ko, O.O. Park, D. W. Kim, "*Capacitance properties of graphite/polypyrrole composite electrode prepared by chemical polymerization of pyrrole on graphite fiber*" *Journal of Power Sources*, vol. 105, pp.20-25, 2002.
- [34] V. Subramanian, H. W. Zhu, R. Vajtai, P. M. Ajayan, B. Q. Wei, "*Hydrothermal synthesis and pseudocapacitance properties of MnO₂ nanostructures*" *Journal of Physical Chemistry B*, vol. 109, pp. 20207-20214, 2005.
- [35] Q. Cheng, J. Tang, J. Ma, H. Zhang, N. Shinya, L. C. Qin, "*Graphene and nanostructured MnO₂ composite electrodes for supercapacitors*" *Carbon*, vol. 49, pp. 2917-2925. 2011.
- [36] P.A. Mini, A. Balakrishnan, S. V. Nair, K.R.V. Subramanian, "*Highly super capacitive electrodes made of graphene/polypyrrole*" *Chemical Communications*, vol. 47, pp. 5753-5755, 2011.

Chapter 2

ELECTROCHEMICAL BEHAVIOR OF SINGLE-WALLED CARBON NANOTUBE SUPERCAPACITORS UNDER COMPRESSIVE STRESS

2.1 Significance

Portable personal electronic devices, micro-electro-mechanical-systems (MEMS), and wireless sensor networks all require microscale energy storage devices that have compact size and lightweight. In addition, some applications also demand for flexibility, stretchability and even bio-compatibility for emerging epidermal electronics [1], which are challenging for suitable electrode/electrolyte combinations and packaging for small scale supercapacitors.

2.2 Literature Review of the Flexible Supercapacitor

In order to make lightweight and flexible supercapacitors, it is suggested that the electrode materials to be toxic free with high gravimetric and volumetric energy/power density. Great efforts have been undertaken, by using CNTs or graphene electrodes, owing to their high flexibility, and high conductivity.

Recently, the printable/brush-on flexible supercapacitor based on CNTs [2,3,4] have been studied, because the technique can reduce the cost and provide a large throughput. Similarly, Pushparaj et al.[5] used nanoporous cellulose paper embedded

with aligned CNT electrode and investigated the performance of the cell with different electrolytes. Wang et al. [6] used ‘domino pushing’ method to manipulate the aligned CNT arrays to become aligned thick buckypaper with better thermal and electrical conductive properties.

Other than CNT paper/textile based electrode, another important candidate to make flexible supercapacitor is graphene/graphene oxide sheet, which exhibits excellent tensile modulus up to 35 GPa and room temperature electrical conductivity of 7200 S m^{-1} .

Except the advancement of flexible electrode, research has been done to understand the mechanism of the flexible supercapacitor during their usage under different ambient conditions, such as the temperature effect [7]. In this work, we successfully investigated the effect of compressive pressure between two SWNT electrodes on the electrochemical performance of the flexible supercapacitors laminated in a plastic package with seven different kinds of aqueous electrolyte solutions. The correlation between the applied pressure and different electrolyte ions as well as its corresponding electrochemical performance is thoroughly investigated.

2.3 Experimental Section

2.3.1 Fabrication of the SWNT Macro-film Electrodes

The freestanding SWNT macro-films were fabricated using a facile chemical vapor deposition (CVD) technique in a tube furnace [8]. A mixture of ferrocene as carbon feedstock/catalyst and sulfur as an additive to promote SWNTs growth at an atomic ratio of Fe: S=10: 1 was heated (1140°C) while a mixture of argon (1500 mL min⁻¹) and hydrogen (150 mL min⁻¹) gas flow was input into the tube furnace. After 50-70 min reaction, the furnace was cooled to room temperature. The freestanding SWNT macro-films were then collected from the two ends of the furnace. In order to eliminate the contamination such as amorphous carbon and the catalytic iron particle, the as-deposited SWNT macro-films were heat-treated in the air at 440 °C for 30 min, and then rinsed with diluted hydrochloric acid for 8 hrs. This purification procedure also significantly increased the number of functional groups (e.g. O=C-OH) within the films. After the acid-wash step, SWNT films were thoroughly washed with DI water. After drying the films in the air for 8 hrs, two 0.5 inch diameter electrodes were punched with an arch punch. The surface morphology of the SWNT electrode was analyzed by JEOL JSM-7400F Scanning Electron Microscope (SEM), as shown in Fig. 2.1.

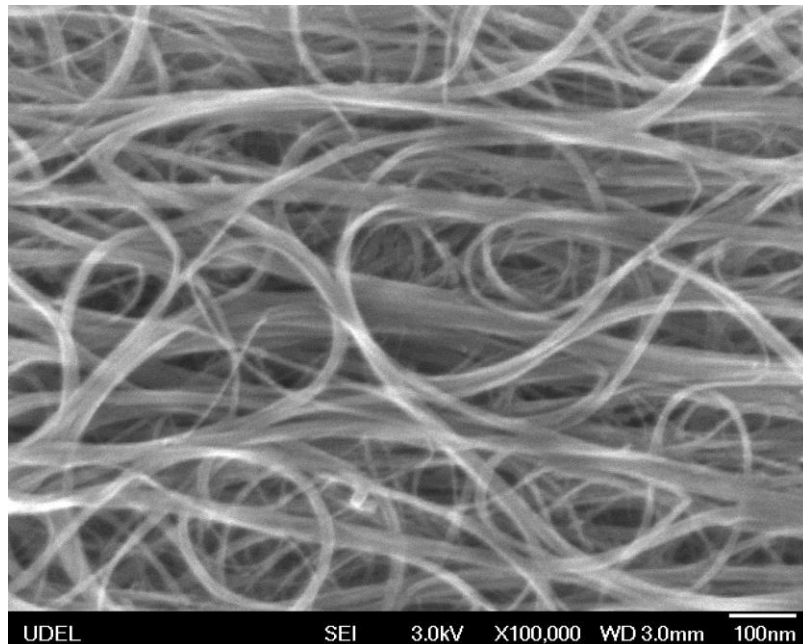


Figure 2.1 SEM of SWNT macro-film after heat and acid treatment.

2.3.2 Flexible Supercapacitor Assembly

The flexible supercapacitor was assembled in a plastic package. A Whatman glass microfiber filter was used as the separator between the two SWNT electrodes. As shown in the schematic of Fig. 2.2a, the supercapacitors were assembled by placing the sandwich-structured core components of a pair of SWNT electrodes separated by the aqueous electrolyte soaked separator. Nickel foils were cut to suit the shape of the core components as the current collectors, which were connected to the testing system under the circumstances of the differently applied pressures to perform a real time measurement of the electrochemical performance of the SWNTs supercapacitor. Fig.

2.2b shows the digital camera image of the flexible supercapacitor. Fig. 2.2c shows the schematic of how the pressure is applied on the flexible supercapacitor.

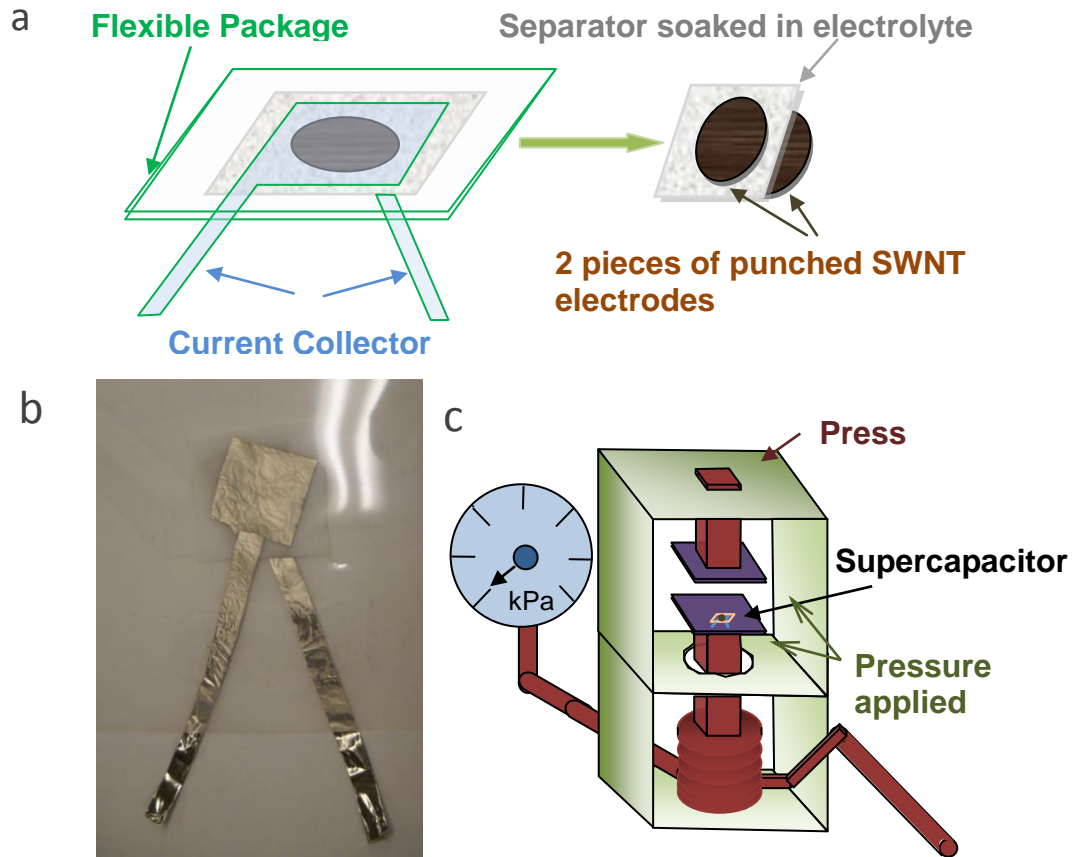


Figure 2.2 (a) Schematic of supercapacitor assembly with SWNT electrodes. (b) Digital camera image of assembled flexible supercapacitor. (c) Schematic of pressure applied facility on supercapacitor.

2.3.3 Electrochemical Measurements

In order to establish the correlation between the applied pressure and different electrolyte ions, 1 M aqueous solutions of LiOH, NaOH, KOH, LiCl, NaCl, KCl, and KNO₃ were used as electrolytes, respectively. The electrochemical characterization under different compressive pressure was done by measuring the cyclic voltammograms (CV) and electrochemical impedance spectra (EIS). The compressive pressure between the electrodes of the SWNT supercapacitors was carefully varied in a controlled manner from 0 to 1723.96 kPa using a Carver hydraulic press. The assembled flexible SWNT supercapacitor was placed in between the parallel plates of the press as shown in Fig. 2.2c. At each applied pressure, the electrochemical cyclic voltammetry and the impedance spectroscopy were characterized with an ET&G PARSTAT 2273 potentiostat/galvanostat.

2.3.4 Contact Angle Measurements

The contact angle measurements were performed using a Rame-Hart Goniometer (model 100-00-115) at room temperature and under atmosphere pressure. Drops of aqueous electrolyte were placed on the surface of the SWNT films (same as the electrode materials) to determine the wetting characteristics.

2.4 Results and Discussion

2.4.1 Pressure Effect on the Specific Capacitance

As previously shown in Fig. 2.1, the SWNT film demonstrates structural combination of a mesoporous material and a macroporous material, allowing aqueous-based electrolyte ions to be able to penetrate inside the film to fully utilize all the effective surface area. Compared with nanoporous materials, counter ions are expected to quickly reside at the electrode/electrolyte interface without having to enter the pores, leading to an exohedral supercapacitor with a high power density feature [9].

Fig. 2.3 shows the specific capacitance values of the capacitors obtained from the voltammograms measured (Fig. 2.4) at increasing pressures with 1 M different aqueous electrolytes, which are separated into two groups base on their pressure dependence performance. Fig. 2.4 a-g display the CV curves of 1 M LiOH, NaOH, KOH, LiCl, NaCl, KCl, and KNO₃ aqueous electrolytes under different pressures, respectively. For group A electrolytes with hydrated hydroxyl anions (OH⁻), the initial specific capacitance is all extremely low (LiOH= 2.7F g⁻¹, NaOH= 3.7 F g⁻¹, KOH=3.6 F g⁻¹) under a pressure of 2.55 kPa. In addition, they showed a quick increase before reaching a saturation stage at pressure of approximately 70 kPa, and saturated with the stable specific capacitance value in a sequence of LiOH (25.0 F g⁻¹) > NaOH (19.7 F

g^{-1}) > KOH (17.4 F g^{-1}) under a pressure of 1723.96 kPa. In contrast, for group B electrolytes with hydrated chloride anion (Cl^-) and hydrated nitrate anion (NO_3^-) (Fig.2.3b), the initial specific capacitance is much higher (LiCl= 28 F g^{-1} , NaCl= 14.9 F g^{-1} , KCl= 14.9 F g^{-1} , KNO_3 = 19.7 F g^{-1}). Moreover, the specific capacitance values are more stable with increasing pressure. Under a pressure of 1723.96 kPa, the capacitances of group B are in a sequence of LiCl (41.4 F g^{-1})> KNO_3 (21.4 F g^{-1})>NaCl (20.6 F g^{-1})>KCl (18.0 F g^{-1}), showing similar sequence as group A in terms of cations. It is also noticed that with same cation (K^+), the capacitance values are in a sequence of KNO_3 (21.4 F g^{-1})>KCl (18.0 F g^{-1})> KOH (17.4 F g^{-1}).

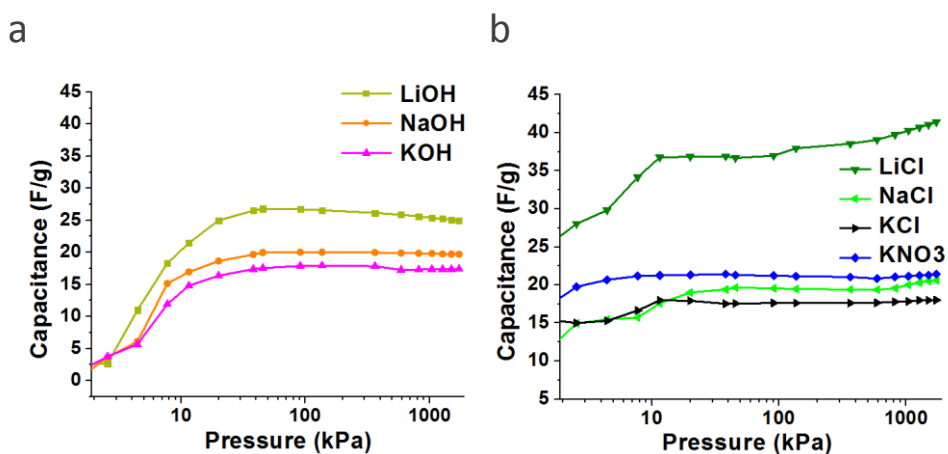


Figure 2.3 Specific capacitance increase trend under pressure effect for electrolytes. (a) LiOH, NaOH, KOH. (b) LiCl, NaCl, KCl, and KNO_3

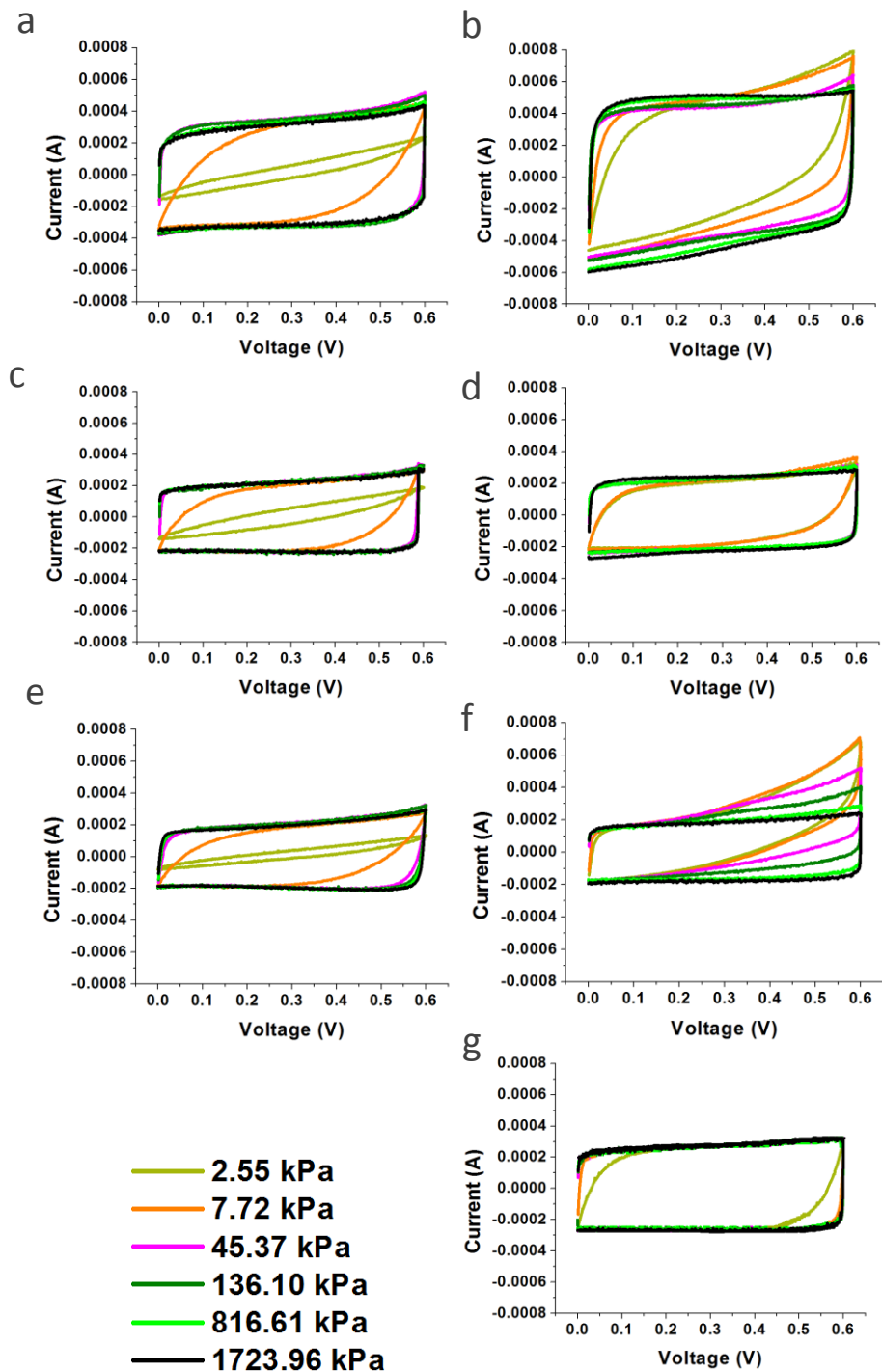


Figure 2.4 Cyclic voltammetry at 50 mV s⁻¹ of the SWNT supercapacitors with 1 M electrolyte under increasing applied pressure (kPa). (a) LiOH (b) LiCl (c) NaOH (d) NaCl (e) KOH (f) KCl (g) KNO₃.

2.4.2 Ion Size Effect and Surface Wettability Effect for Different Electrolyte

The reasons for these results are attributed to the different interfacial wettability of solutions at the electrode/electrolyte interface caused by different ions as well as size differences among the hydrated ions. Surface wettability was firstly under close scrutiny as one important aspect for governing the supercapacitor performance [10]. In order to accurately evaluate the surface wettability of the different electrolytes on the SWNT films, the contact angle of each electrolyte was measured by goniometer and the results are shown in Table 2.1.

Table 2.1 Contact Angle of Different 1 M Electrolyte on the Surface of SWNT Electrode

Electrolyte	Contact angle (degree)	Electrolyte	Contact angle (degree)
KOH	60	LiOH	60
KCl	54	NaOH	60
KNO ₃	45	Water	36

It is well known that the surface tension of solution (γ_{soln}) and the surface tension of water (γ_{H_2O}) hold the following Equation (2.1):[11]

$$\gamma_{soln} - \gamma_{H_2O} = gm_a \quad (2.1)$$

where m_a is the molar concentration of the anions (the role of cations is not significant, as confirmed from our contact angle results), and g is the slope, which can be calculated by Equation (2.2):

$$g = a + (bz/r_a) \quad (2.2)$$

where z is charge of the anion, r_a is the radius of the anion (Å), a and b are coefficients. The slope (g) of related anions has been studied by Abramzon et al,[12] as shown in Table 2.2.

Table 2.2 Slope (g) of the surface tension equation

Anion	g (mNm ⁻¹ kg-mol ⁻¹)
OH ⁻	2.00
Cl ⁻	1.57
NO ₃ ⁻	1.23

The numerical value of surface tension in terms of anions indicates OH⁻>Cl⁻>NO₃⁻, in good agreement with the experimental data from the contact angle measurements. It is also in correlation with the specific capacitance of different electrolytes under an increasing pressure. For instance, electrolyte with OH⁻ anions has the largest contact angle, indicating a poorer surface wettability compared to electrolytes with Cl⁻ and NO₃⁻ anions and resulting in a lower specific capacitance under the same pressure.

For electrolytes with same anions, e.g. OH⁻ or Cl⁻, the contact angle as well as the surface tension is relatively the same, however, there are still differences among the electrolytes in terms of capacitive behavior, where hydrated ion size (namely hydrated Li⁺, Na⁺, and K⁺) of the electrolytes becomes the dominating factor after the surface wettability property. For exohedral supercapacitors, the counterions are

accumulated in the double layer mainly by electrostatic forces at the distance of outer Helmholtz plane [9]. Theoretically, the higher the surface area is, and the higher amount of the charged ions that can access to the electrode/electrolyte interface, the higher capacitance value the supercapacitor has[10]. For aqueous electrolytes, the hydrated ion sizes can simply be estimated with Equation (2.3):

$$d_{ion} = 0.1376 + 1.0167r_p \quad (2.3)$$

where d_{ion} is the average distance between ions and the nearest water molecules, r_p is the Pauling ionic radii (Table 2.3). The hydrated ion size is determined by the diameter of the ion, which should be $2d_{ion}$.

Table 2.3 Pauling ionic radii (r_p), hydrated ion size ($2d_{ion}$), Capacitance under 1723.96 kPa

Cation	r_p (nm)	$2d_{ion}$ (nm)	Capacitance with OH ⁻ anions (F g ⁻¹)	Capacitance with Cl ⁻ anions (F g ⁻¹)
Li ⁺	0.060	0.397	25.0	41.4
Na ⁺	0.095	0.468	19.7	20.6
K ⁺	0.133	0.546	17.4	18.0

Table 2.3 shows that with the decrease of the ion size ($K^+ > Na^+ > Li^+$), the capacitance will increase due to the straightforward reason that more charged cations can access to the electrode/electrolyte interface and contribute to the charge storage. This phenomenon is experimentally proved by the specific capacitance values under the saturation stage, after the surface wettability is improved by the compressive pressure

applied on the supercapacitors, in both electrolytes with OH^- anions (Fig. 2.3a) and Cl^- anions (Fig. 2.3b).

The surface wettability effect determined by anions and ion-size effect determined by cations on the capacitive performance of the SWNT supercapacitors are evidenced by the CV curves, as shown in Fig. 2.4. The initially poor wettability of electrolytes with OH^- anions was evidenced by the distorted CV curves and low capacitance values under pressure below approximately 70 kPa. However, for electrolytes with Cl^- and NO_3^- anions, which have a better wettability, the CV curves showed less distortion with relatively larger areas than those with OH^- anions under the same pressure. It was also evidenced that the compressive pressure improves the surface wettability for all electrolytes, especially for electrolytes with the OH^- anions. CV curves under pressures above approximately 70 kPa are close to rectangular shape for all electrolytes, indicating the capacitors are approaching to an ideal capacitive behavior. The compressive pressure induced phenomenon can be further explained in detail by the electrochemical impedance spectroscopy (EIS) measurements presented below.

2.4.3 Electrochemical Impedance Spectroscopy Study

The primary objective of the EIS measurements is to gain insight into the pressure dependence of the capacitive and resistive elements and their effects on the performance of the supercapacitors. Fig. 2.5 and Fig. 2.6 show the impedance results of Nyquist spectra in the frequency range from 100 kHz to 10 mHz measured at

equilibrium open circuit potential (~ 0 V) under a small (Fig. 2.5) and a large (Fig. 2.6) compressive pressure for different electrolytes.

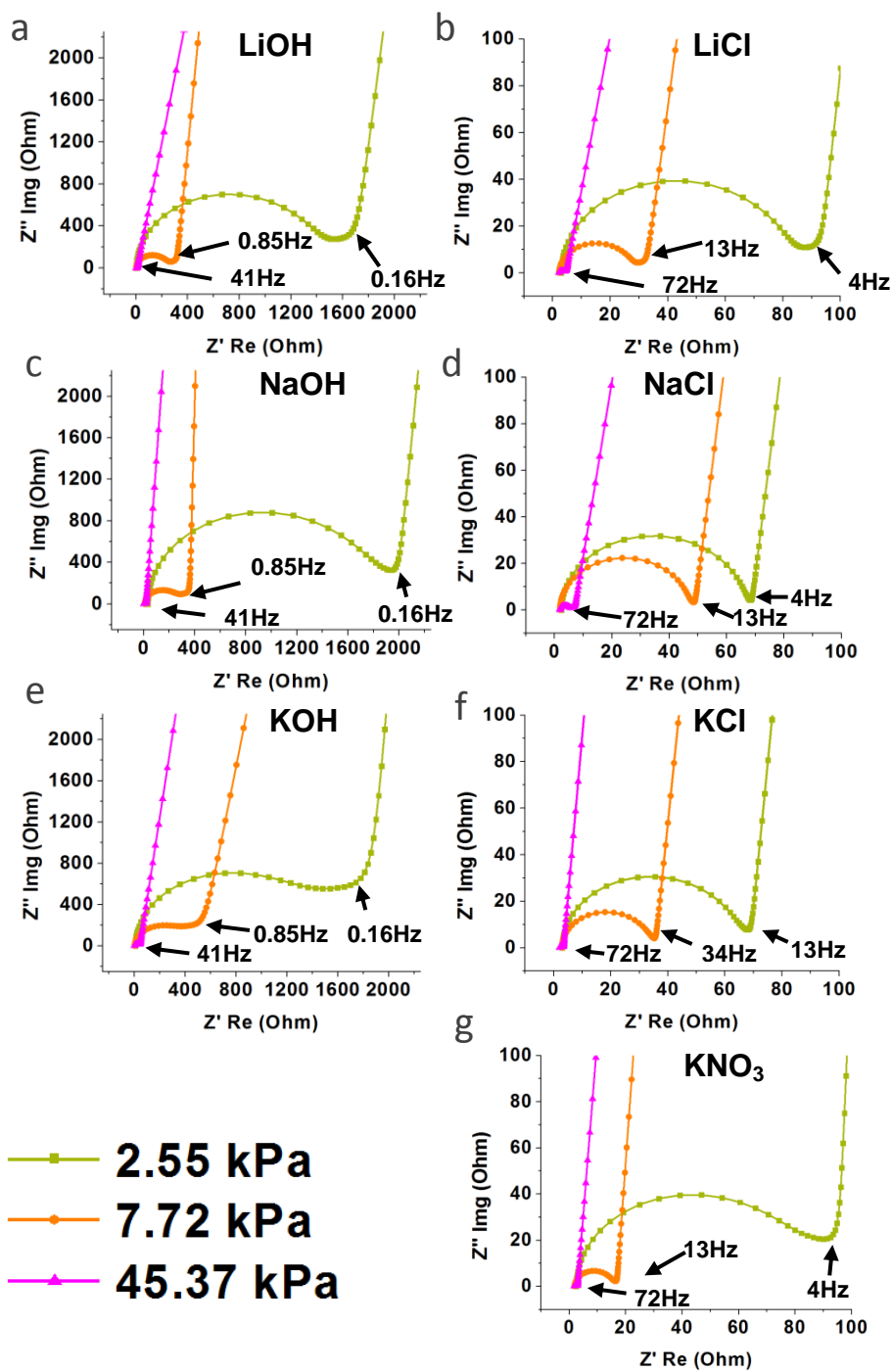


Figure 2.5 Impedance results with "knee" frequency of the SWNT supercapacitors under small applied pressures (a) LiOH (b) LiCl (c) NaOH (d) NaCl (e) KOH (f) KCl (g) KNO₃.

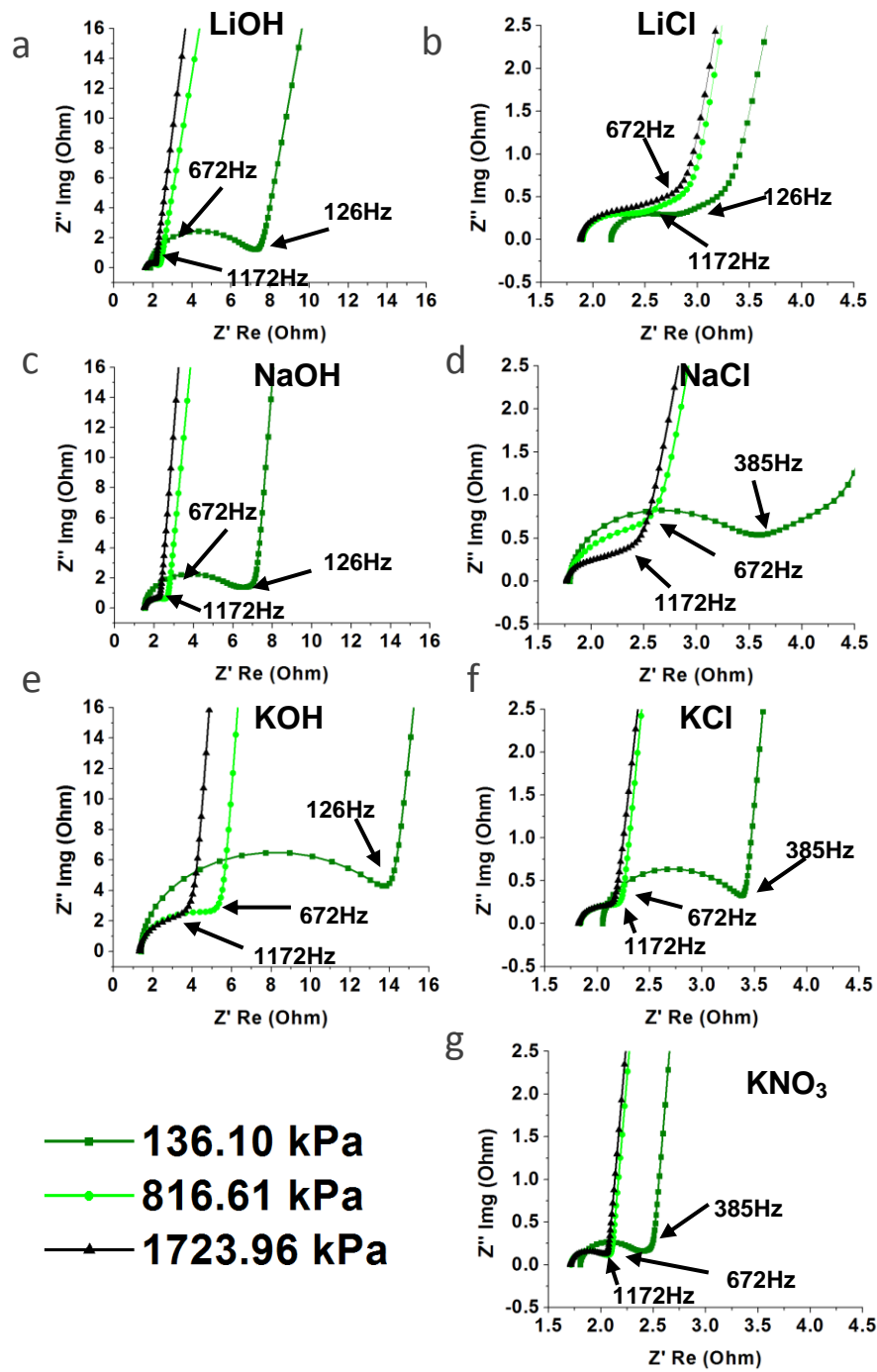


Figure 2.6 Impedance results with "knee" frequency of the SWNT supercapacitors under large applied pressures. (a) LiOH (b) LiCl (c) NaOH (d) NaCl (e) KOH (f) KCl (g) KNO₃.

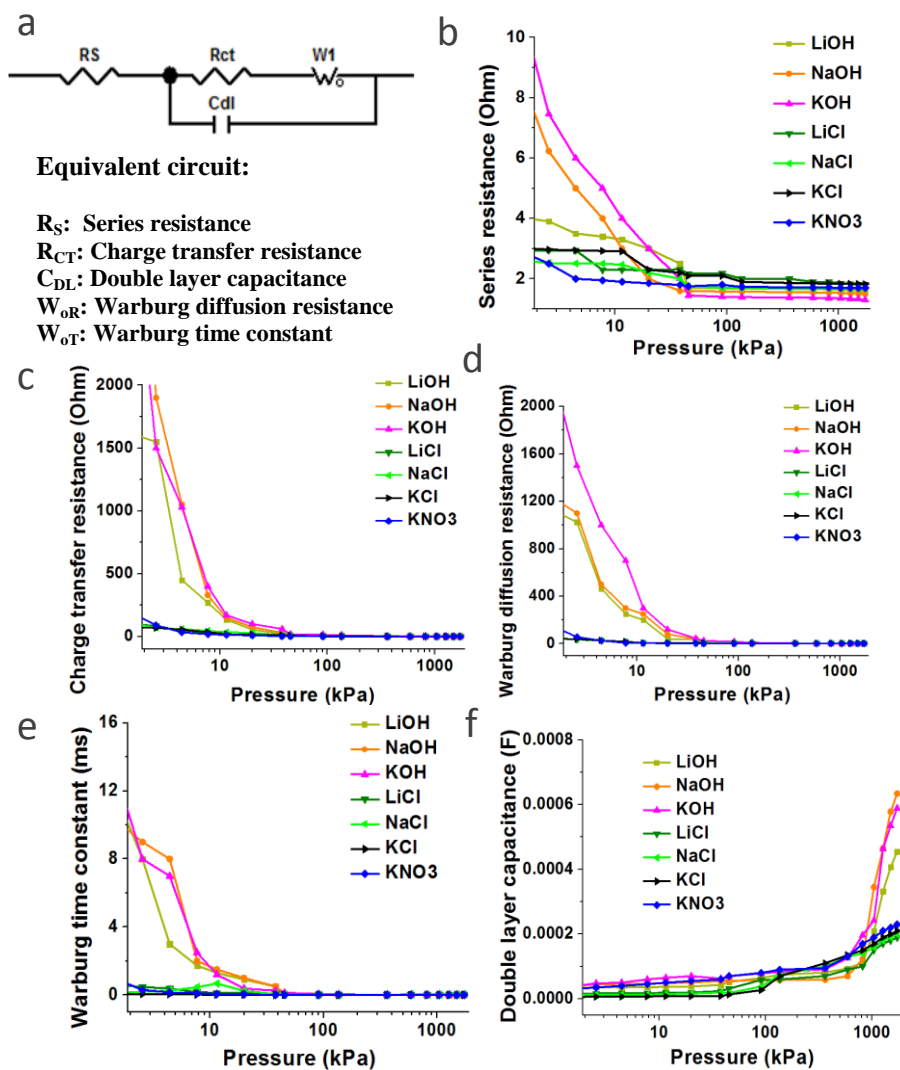


Figure 2.7 Impedance curve fitting results for each element in equivalent circuit (a) AC impedance equivalent circuit. (b) Series Resistance, (c) Charge transfer resistance, (d) Warburg diffusion resistance, (e) Warburg time constant, and (f) Double layer capacitance.

The Nyquist spectrum can be well represented by an equivalent circuit as shown in Fig. 2.7a. The first intersection point on the real axis of the Nyquist spectrum in the high-frequency region provides the value of the electrolyte resistance, the intrinsic resistance of the active electrode material, and the contact resistance at the interface of active material/current collector, defined as series resistance R_s [13]. The R_s element is in series with the electrical double layer capacitance at the interface of electrode and electrolyte C_{DL} [14]. C_{DL} is in parallel with the charge-transfer resistance R_{ct} and Warburg impedance W_o . R_{ct} shown as the second intersection point of the semi-circle on the real axis represents the total resistance at the interface between the electrode and electrolyte [15]. It should be noted that throughout the experiments, the current collector (Ni foils) and the SWNT electrode materials were well attached together following the same manner. It is speculated that the variation of the contact resistance between the Ni foil and the SWNT film with respect to the pressure change was the same; all the variation associated with the impedance variation should be attributed to the intrinsic difference of each electrolyte and the properties of electrode/electrolyte interface.

Typically, the Nyquist spectrum is divided into two regions by the "knee" frequency [16, 17], where the high frequency semi-circle is attributed to the charge transfer process occurring at the electrode-electrolyte interface[18], and the low frequency curve with its slope gradually changing from 45° to 90° represents the Warburg finite-length diffusion stage when ions diffuse within the electrode[19].

Experimental results show that the "knee" frequency increases with the applied pressure for all electrolytes, as summarized in Table 2.4.

Table 2.4 Knee frequency (experiment data) vs. Pressure

Pressure (kPa)	Knee frequency (Hz)						
	LiOH	NaOH	KOH	LiCl	NaCl	KCl	KNO ₃
2.55	0.16	0.16	0.16	4	4	13	4
7.72	0.85	0.85	0.85	13	13	34	13
45.37	41	41	41	72	72	72	72
136.10	126	126	126	385	385	385	385
816.61	672	672	672	672	672	672	672
1723.96	1172	1172	1172	1172	1172	1172	1172

Table 2.4 shows that the “knee” frequency increase caused by the applied pressure presents a significant high frequency of 1172 Hz for all electrolytes under the maximum pressure at 1723.96 kPa. This value suggests that under the pressure, the electrical energy can be stored in the double-layer capacitor at frequency up to 1172 Hz, significantly higher than reported supercapacitors assembled with other electrode materials (a few Hz to 300 Hz) [16,17], indicating an excellent high-power capability. The high "knee" frequency could be resulted from the pressured induced easy accessibility of ions at the electrolyte/electrode interface and excellent electric conductivity from the SWNT films. It is noted that the semi-circle in the high frequency region (Fig. 2.6) almost disappeared under a pressure higher than 816.61 kPa. The absence of the semi-circle in the complex impedance plane implies a very good ionic conductivity at the electrode/electrolyte interface [20,21].

Fig. 2.7 shows pressure dependence of all the curve fitting values of R_s , R_{CT} , C_{DL} , W_{OR} and W_{OT} of the experimental impedance spectra based upon the proposed equivalent circuit (Fig.2.7a). During the initial stage with a relatively low applied pressure, it is interesting to notice that the charge transfer resistance of all the electrolytes with OH^- anions is 10 fold higher than that of the electrolytes with Cl^- or NO_3^- anions. As the charge transfer resistance decreased with gradual pressure increase, the specific capacitance increased in all electrolytes. However, the decreasing scale for the OH^- electrolytes is much more significant than that of Cl^- or NO_3^- . This is because of the much improved surface wettability. For instance, the charge transfer resistance decreases from 1550 ohm to 270 ohm (by 82%) for LiOH electrolyte when the applied pressure increases from 2.55 kPa to 7.72 kPa, resulting in the sharp increase of the specific capacitance from $2.66 F g^{-1}$ (under a pressure of 2.55 kPa) to $18.31 F g^{-1}$ (under a pressure of 7.72 kPa). While the charge transfer resistance decreases by 65% from 85 ohm to 30 ohm for the LiCl electrolyte under the same applied pressures, resulting in the specific capacitance increase from $28.03 F g^{-1}$ (under a pressure of 2.55 kPa) to $34.15 F g^{-1}$ (under a pressure of 7.72 kPa). When a large pressure applied, all dominant factors to determine capacitance (series resistance, charge transfer resistance, and Warburg diffusion resistance) reach saturation stage for all electrolytes. Little improvement on the decrease of the charge transfer resistance (Fig.2.7c) cannot bring much ameliorative effect to improve the specific capacitance.

In addition, the pressure increase greatly reduces the Warburg diffusion resistance (W_{OR}) and Warburg time constant (W_{OT}), especially for group A

electrolytes, as shown in Fig. 2.7d and Fig. 2.7e, respectively. The initial value of Warburg diffusion resistance is extremely large, indicating difficult ion diffusion within the electrode. In general, the ions diffuse easier and quicker into the SWNT electrode materials with a better surface wettability Cl^- and NO_3^- electrolytes than that with the poor surface wettability OH^- anions electrolyte.

For the applied pressures above approximately 70 kPa, the impedance and CV curves as well as the specific capacitance change little in the supercapacitors using SWNT electrodes. This phenomenon is different from that using other pore-structured electrode materials, such as activated carbon fibers, where the specific capacitances continuously increase even up to 2068.43 kPa, revealing that SWNTs distinguish themselves from typical micro-porous structured materials when they are utilized as electrode materials for supercapacitors.

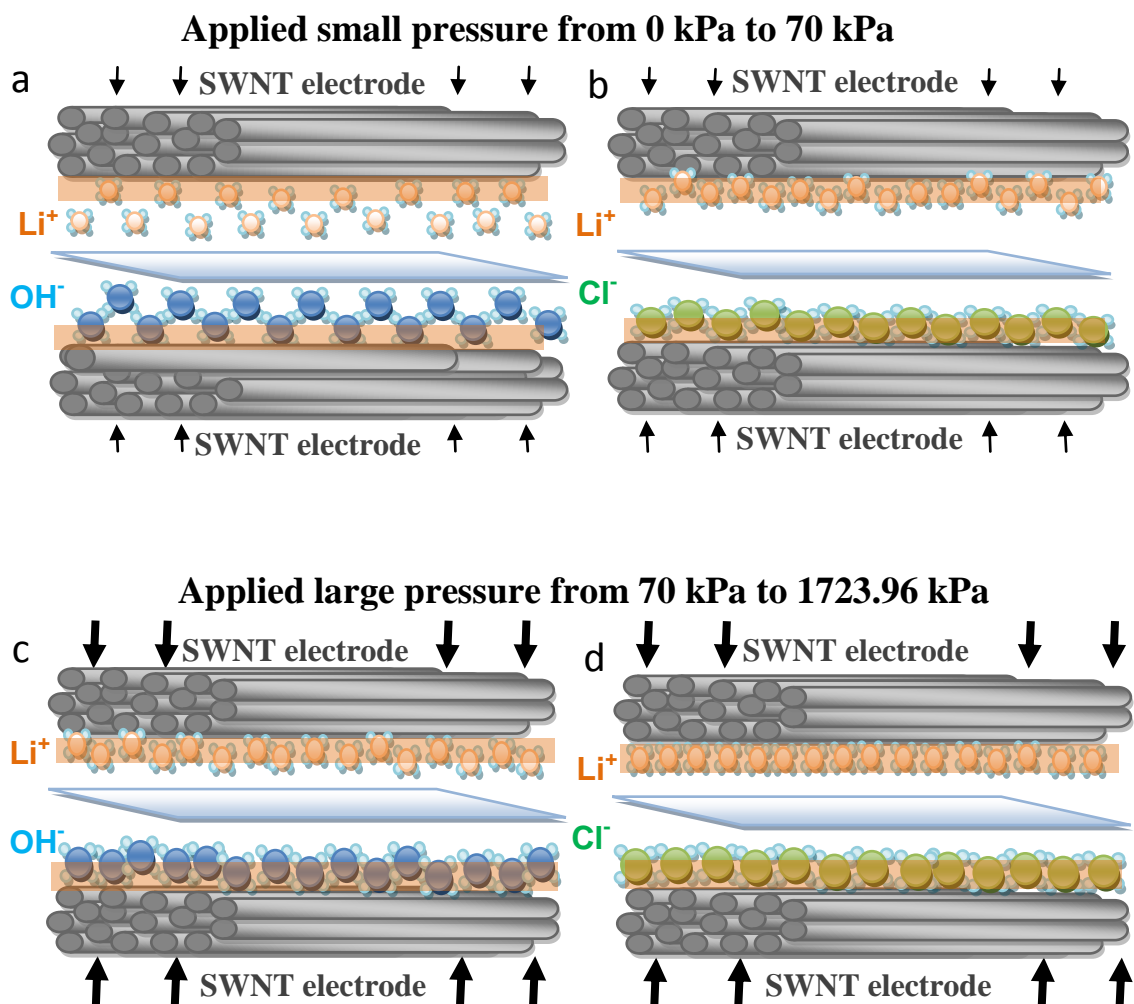


Figure 2.8 Schematic representation of the cations/anions in aqueous electrolyte/SWNT electrode interface during the pressure increase process with Helmholtz planes presented by the semitransparent orange band. (a) LiOH under small pressure, (b) LiCl under small pressure, (c) LiOH under large pressure, and (d) LiCl under large pressure.

In the current experiments, the different pressure dependence behavior of the quick capacitance saturation for group B electrolytes (with Cl⁻ or NO₃⁻ anions) and the

drastic capacitance increase for group A electrolytes (with OH^- anions), before reaching the critical pressure around 70 kPa, can be visually explained using the schematic shown in Fig. 2.8. The schematic illustrates the difference of group A and group B electrolytes under small and large applied pressures. To begin with a low pressure (less than approximately 70 kPa) circumstance, the anions as well as the cations are not stabilized well within the Helmholtz layer at the electrode/electrolyte interface due to the poor wettability for the group A electrolytes with OH^- anions (Fig. 2.8a). Most of the charged anions and cations are freely floating inside the aqueous electrolyte without getting well attached to the surface of the SWNT electrodes. In contrast, the anions (Cl^- and NO_3^-) and cations from group B (Fig. 2.8b) are more affinitive to the surface of the SWNT electrodes due to a better surface wettability (confirmed by the contact angle measurements), thus bringing a much lower initial charge transfer resistance and a higher specific capacitance than their counterparts from group A. In terms of the ion-size effect, it is well understood that smaller cations (Li^+) take less space when residing on the electrode surface and bring a much higher specific capacitance than larger size cations (Na^+ and K^+).

This study clearly presents that SWNT electrodes are excellent materials for flexible supercapacitors and can withstand pressures as high as 1723.96 kPa, while still performing well within the cell package. It also shows the importance of the applied pressure between the SWNT electrodes and its critical influence on the properties of electrolyte anions and cations, which play governing roles in terms of the surface wettability, impedance behavior, the specific capacitance, as well as the high-

power capability for rapid charge/discharge of supercapacitors. The results derived from the pressure dependent measurements on SWNT electrode supercapacitors can have a potential impact on supercapacitor assembly and packaging. They provide valuable information on electrode materials selection and electrolytes with suitable cation and anion properties in order to achieve the optimized capacitor performance with minimal resources, especially for perspective flexible/stretchable supercapacitors, where the pressure variation between the electrodes will be unavoidable. The variation in capacitance of a flexible supercapacitor, with the application of any deformation in usage, can then be understood with the knowledge of either an increase or decrease in the pressure between the electrodes as a result of deformation. In addition, the stability of the electrode material is of great importance to maintain stable electrochemical performance with varying applied strains in a flexible supercapacitor.

2.5 Conclusions

In summary, pressure dependence between the electrodes on the electrochemical performance of the flexible supercapacitors assembled with SWNT electrodes in various aqueous electrolytes has been demonstrated. The specific capacitance increase in various scale with the increase of pressure depending on electrolytes. For the supercapacitors with hydrated hydroxyl anions (OH⁻), the capacitance drastically increased till reaching a saturation stage due to an improved surface wettability of the electrolytes on the SWNT electrodes. For the supercapacitors

with hydrated chloride anions (Cl⁻) and nitrate anions (NO₃⁻), the capacitance saturated earlier due to the better surface wettability. Smaller ion-size cation leads to a higher specific capacitance, indicating that the ion-size effect plays an important role to determine the specific capacitance. In addition, the increased pressure also brings an improving effect on the "knee" frequency, which makes the flexible supercapacitor capable of storing electrical energy at significantly higher frequencies up to 1172 Hz. The fundamental understanding of the research work therefore demonstrates the ameliorative effect of compressive pressure on the SWNTs supercapacitors and provides guidelines for future design of next generation flexible/stretchable supercapacitors.

REFERENCES

- [1] D. Kim, N. Lu, R. Ma, Y. Kim, S. Wang, J. Wu, S.M. Won, H. Tao, A. Islam, K.J. Yu, T. Kim, R. Chowdhury, M. Ying, L. Xu, M. Li, H. Chung, H. Keum, M. McCormick, P. Liu, Y. Zhang, F. G. Omenetto, Y. Huang, T. Coleman, J. Rogers, "*Epidermal electronics*" *Science*, vol. 333, pp.838-843, 2011.
- [2] M. Kaempgen, C. K. Chan, J. Ma, Y. Cui, G. Gruner, "*Printable thin film supercapacitors using single-walled carbon nanotubes*" *Nano Letters*, vol. 9, pp. 1872-1876, 2009.
- [3] L. Hu, H. Wu, Y. Cui, "*Printed energy storage devices by integration of electrodes and separators into single sheets of paper*" *Applied Physics Letter*, vol.96, 183502, 2010.
- [4] Q. Liu, M. H. Nayfeh, S. T. Yau, "*Brushed-on flexible supercapacitor sheets using a nanocomposite of polyaniline and carbon nanotubes*" *Journal of Power Source*, vol. 195, pp.7480–7483, 2010.
- [5] V. L. Pushparaj, M. M. Shaijumon, A. Kumar, S. Murugesan, L. Ci, R. Vajtai, R.J. Linhardt, O. Nalamasu, P.M. Ajayan, "*Flexible energy storage devices based on nanocomposite paper*" *Proceedings of the National Academy of Sciences*, vol. 104, pp. 13574–13577, 2007.
- [6] D. Wang, P.C. Song, C. H. Liu, W. Wu, S.S. Fan, "*Highly oriented carbon nanotube papers made of aligned carbon nanotubes*", *Nanotechnology*, vol. 19, pp. 075609, 2008.
- [7] C. Masarapu, H.F. Zeng, K.H. Hung, B.Q. Wei, "*Effect of temperature on the capacitance of carbon nanotube supercapacitors*" *ACS Nano*, vol. 3, pp. 2199-2206, 2009.
- [8] H.W. Zhu, B.Q. Wei, "*Direct fabrication of single-walled carbon nanotube macro-films on flexible substrates*" *Chemical Communications*, vol. 29, pp.3042–3044, 2007.

- [9] J.S. Huang, B.G. Sumpter, V. A. Meunier, "A universal model for nanoporous carbon supercapacitors applicable to diverse pore regimes, carbon materials, and electrolytes", *Chemistry - A European Journal*, vol.14, pp. 6614-6626, 2008.
- [10] E. Frackowiak, F. Beguin, "Electrochemical storage of energy in carbon nanotubes and nanostructured carbons" *Carbon*, vol.40, pp. 1775, 2002.
- [11] A.L. Horvath, "Handbook of aqueous electrolyte solutions: physical properties, estimation and correlation methods", Ellis Horwood Limited, UK, 1985.
- [12] A.A. Abramzon, S.I. Kol'tsov, I.A. Murashev, "Surface tension of aqueous solutions of inorganic salts", *Russian Journal of Physical Chemistry*, vol.56, pp.86-89, 1982.
- [13] Q. Wu, K. He, H. Mi, X. Zhang, "Electrochemical capacitance of polypyrrole nanowire prepared by using cetyltrimethylammonium bromide (CTAB) as soft template", *Materials Chemistry and Physics*, vol. 101, pp. 367-371, 2007.
- [14] B. E. Conway, "Electrochemical supercapacitors: scientific fundamentals and technological applications" Kluwer Academic and Plenum, New York, 1999.
- [15] C.Z. Yuan, X.G. Zhang, Q.F. Wu, B. Gao, "Effect of temperature on the hybrid supercapacitor based on NiO and activated carbon with alkaline polymer gel electrolyte" *Solid State Ionics*, vol. 177, pp. 1237-1242, 2006.
- [16] C.C.Hu, C.C. Wang, "Nanostructures and capacitive characteristics of hydrous manganese oxide prepared by electrochemical deposition" *Journal of The Electrochemical Society*, vol. 150, pp. A1079-A1084, 2003.
- [17] D.A. Brevnov, T.S. Olson, "Double-layer capacitors composed of interconnected silver particles and with a high-frequency response" *Electrochimica Acta*, vol. 51, pp.1172-1177.2006.
- [18] J. Gamby, P.L. Taberna, P. Simon, J.F. Fauvarque, M. Chesneau, "Studies and characterisations of various activated carbons used for carbon/carbon supercapacitors" *Journal of Power Sources*, vol. 101, pp.109-116,2001.
- [19] W. Sugimoto, K. Yokoshima, Y. Murakami, Y. Takasu, "Charge storage mechanism of nanostructured anhydrous and hydrous ruthenium-based oxides", *Electrochimica Acta*, vol.52, pp.1742-1748, 2006.

[20] J. Chmiola, G. Yushin, Y. Gogotsi, C. Portet, P. Simon, P.L. Taberna, "Anomalous increase in carbon capacitance at pore sizes less than 1 nanometer" *Science*, vol.313, pp. 1760-1763, 2006.

[21] R. Lin, P.L. Taberna, L. Chmiola, D. Guay, Y. Gogotsi, P. Simon, "Microelectrode study of pore size, ion size, and solvent effects on the charge/discharge behavior of microporous carbons for electrical double-layer capacitors" *Journal of the Electrochemical Society*, vol.156, pp. A7-A12, 2009.

Chapter 3
DYNAMIC STRETCHABLE SUPERCAPACITOR BASED ON BUCKLED
SINGLE-WALLED CARBON NANOTUBE MACORFILMS AND
ELASTOMERIC SEPARATOR

3.1 Significance

The stretchable electronics [1] [2] are emerging as a new technological advancement after flexible electronics; they can endure much higher strain while maintaining their functionality, which provide grounds for the invention of new applications, such as epidermal electronics [3]. As pointed out in Chapter 2, the flexible supercapacitors have been studied by different groups, from different perspective. However, the research on the stretchable supercapacitor to meet the energy demand from stretchable electronic devices is still not fully developed. Consequently, it is of great important to build the stretchable energy storage device to provide the power to the stretchable electronics, and also investigate their performance under various ambient conditions.

3.2 Literature Review of Stretchable Electronics and Stretchable Energy Storage Devices

To date, stretchable electronic devices have been researched by different groups, such as stretchable organic light-emitting diode (OLED) devices[4,5] with stretchable interconnects[6], loudspeakers[7], pressure and strain sensors[8-10], temperature sensors[11], radio frequency (RF) devices[12], and field effect transistors[13]. In order to power the stretchable electronics, stretchable energy conversion and storage devices become key components to achieve a fully independent and stretchable system. Stretchable energy conversion devices have been reported, such as the stretchable organic solar cell [14], GaAs photovoltaic cell [15], and various piezoelectric devices[16,17]. As for stretchable energy storage devices, there have been recent publications focused on the electrode components, such as the stretchable graphene electrode [18] , the buckled single-walled carbon nanotube(SWNT) electrode [19], the polypyrrole electrode containing the dopant *p*-toluenesulfonate anion (PPy-*p*TS) [20], and the PPy coated nylon lycra fabric electrode[21]. However, the fully stretchable energy storage devices are relatively underdeveloped, with the exception of a newly reported stretchable SWNT/textile composite [22], and an ultracompliant electrochemical dry gel cell [23]. Nevertheless, these stretchable cell reports still have disadvantages or lack detailed results of their functionality during dynamic stretching. For example, the results of the buckled

SWNT supercapacitor only reported the performance of the cell at fixed stretching modes [19]. For a stretchable battery made with the PPy-*p*TS electrode, the whole cell still needs to be immersed in aqueous phosphate buffered saline (PBS) electrolyte during the stretching/releasing (in situ 30% strain) at a 2% s⁻¹ strain rate, which is not feasible for practical purposes. Also, a fully rechargeable PPy-*p*TS based battery has yet to be fabricated[20]. The PPy coated on nylon lycra fabric only achieved the stretchability on the electrode level [21]. The SWNT/textile supercapacitor cell investigated only reported the performance of the cell before and after 100 cycles of stretching, but not the electrochemical performance in situ during the physical stretching and releasing of the cell when the cell is functioning at the charge/discharge cycles [22]. Finally, the stretchable electrochemical dry gel cell reported is non-rechargeable, and the fabrication process is complicated, due to the non-ionic conductive separator and the many layers within the cell [23].

In this study, we demonstrated for the first time a dynamic stretchable energy storage device, with instantaneously monitored electrochemical behavior under dynamic stretching and releasing modes, which reveal the real performance of the stretchable energy storage device during normal operation. The stretchable energy storage device will provide an important power source for future stretchable computers and biomedical applications. The real time dynamic testing method will also provide an important guideline for the design optimization of future stretchable energy storage devices.

3.3 Experimental Section

3.3.1 Compliant Polydimethylsiloxane Substrate Fabrication

The Polydimethylsiloxane (PDMS, Dow Corning Sylgard 184) was prepared by mixing the base and curing agent with a weight ratio of 20:1. The solution was then poured into a petri dish. After 5 minutes of manually mixing, the solution was put into a vacuum chamber to remove any trapped gas created by the mixing. The solution was then cured at 60 °C for 12 hour. The cured PDMS slab with uniform thickness (1 mm) was cut with a razor blade to a length of 5 cm and a width of 3 cm.

3.3.2 Electrospinning of Polyurethane Elastomeric Separator

The polyurethane (PU) elastomeric separator was fabricated using the electrospinning technique [24,25]. PU pellets (Desmopan 9370A, Bayer Material Science LLC) were dissolved with a weight concentration of 10% in a HPLC-grade mixture of tetrahydrofuran (THF, Sigma-Aldrich) and dimethylformamide (DMF, Sigma-Aldrich) (volume ratio of 6:4). The solution was magnetically stirred for 24 hours and then it was transferred to a 20 mL syringe, with a needle attached, for electrospinning. The electrospinning was carried out using a syringe pump, with the flow rate of 30 $\mu\text{L min}^{-1}$. At high working voltage (Gamma High Voltage Research) of 20 kV, the PU solution was electrospun and collected with a non-sticking aluminum

foil, which was situated vertically at a distance of 35 cm from the needle tip. The electrospun PU separator then was cut and peeled from the aluminum foil to be used in the supercapacitor.

3.3.3 Dynamically Stretchable Supercapacitor (DSS) Assembly

A custom-made dynamic movable stage was utilized to pre-stretch the PDMS with 33.3% pre-strain. Then, the pre-strained PDMS was subjected to UV light to produce a chemically activated surface to facilitate the strong bonding with the buckled SWNT film [19]. Next, the freestanding SWNT macrofilms were attached and secured to the PDMS substrate. In order to relieve residual stress in the transverse direction, the SWNT film was cut into strips in the longitudinal direction during the pre-strain stage. Then, the PDMS was released to form the “wavy” structure of the buckled SWNT films. Finally, two PDMS slabs with buckled SWNT films were pressed together with the electrospun PU separator and copper foil strips as current collectors in between. 1 M tetraethylammonium tetrafluoroborate (TEABF₄) dissolved in propylene carbonate (PC) was used as the organic electrolyte. The electrolyte was injected into the DSS to wet the separator after it was placed inside the glove box (Unilab, MBraun) filled with purified argon (both oxygen and water levels are below 0.01 ppm).

3.3.4 Electrochemical Characterization

The cyclic voltammograms (CV) were performed with an EG&G PARSTAT 2273 potentiostat/galvanostat with various scan rates. The AC electrochemical impedance spectroscopy (EIS) was conducted at frequency range from 100 kHz to 10 mHz. The impedance results were fitted using commercial software ZVIEW, to calculate the parameters in the equivalent circuit. The galvanostatic charge-discharge measurements were performed on an Arbin BT4+ test system. The electrochemical performance versus the dynamic strain applied was tested by clamping the DSS onto the programmable stage to apply tensile strain. First, all the electrochemical measurements were performed with DSS fixed statically under 0 % and 31.5 % strain, respectively. Then, the electrochemical measurements were performed while the DSS was being dynamically stretched and released between 0 % and 31.5% strain, with different strain rate applied (1.11 % s⁻¹, 2.22 % s⁻¹, 4.46 % s⁻¹). The electrochemical tests were carried out inside the argon-filled glove box at room temperature.

3.3.5 Morphology Characterization

The scanning electron microscopy (SEM) images of the electrospun PU separator was taken with a JEOL JSM-7400F microscope. The optical image of the

buckled SWNT film was taken with Olympus BX60 microscope and Nikon DS-Fi1 camera.

3.4 Results and Discussion

3.4.1 Concept and Morphology of the Components

The main components of the DSS are depicted in Fig.3.1. In the experiment, copper strips are used as current collector. However, for future applications it is suggested to implement a compliant stretchable interconnect. In the study, the DSS system is subject to an uniaxial stress and thus can be cyclically stretched and released between 0 % (SWNTs were buckled) to 31.5% strain (SWNTs were almost flattened), as shown in Fig. 3.1b.

Fig. 3.2a reveals the SEM image of the electrospun PU elastomeric separator, which has nonwoven porous structure. The fiber diameters range from 0.8 μm to 1.2 μm . The interconnected voids between the fibers create ample space for the mobile ions in the electrolyte to move freely through the membrane, ensuring the good ionic conductivity, and low resistance created by the separator. The electrospinning process provides a relatively uniform membrane that can be easily cut to different shape as an elastomeric separator. For electrochemical testing, the thickness of the electrospun separator is controlled to be 10 μm .

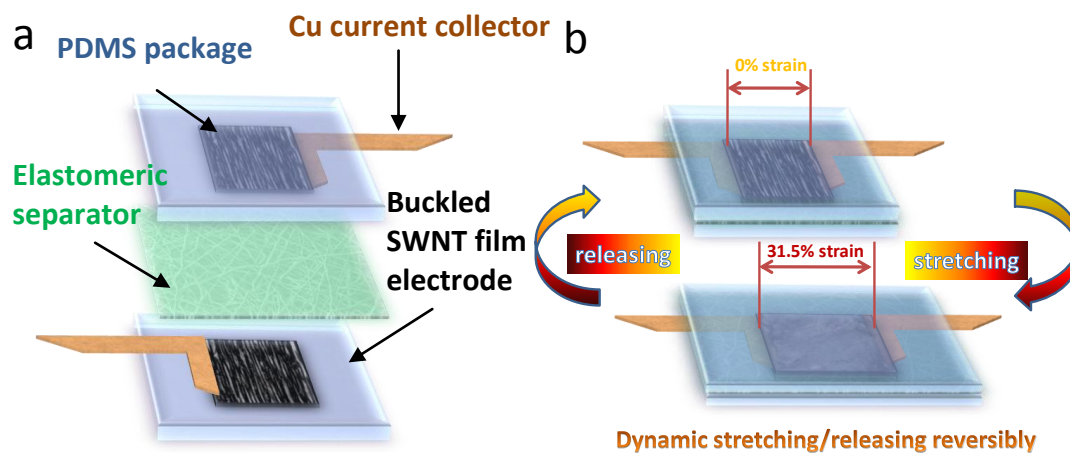


Figure 3.1 a) Schematic of the main components of the DSS. b) Schematic of the DSS under 0% strain and 31.5% strain.

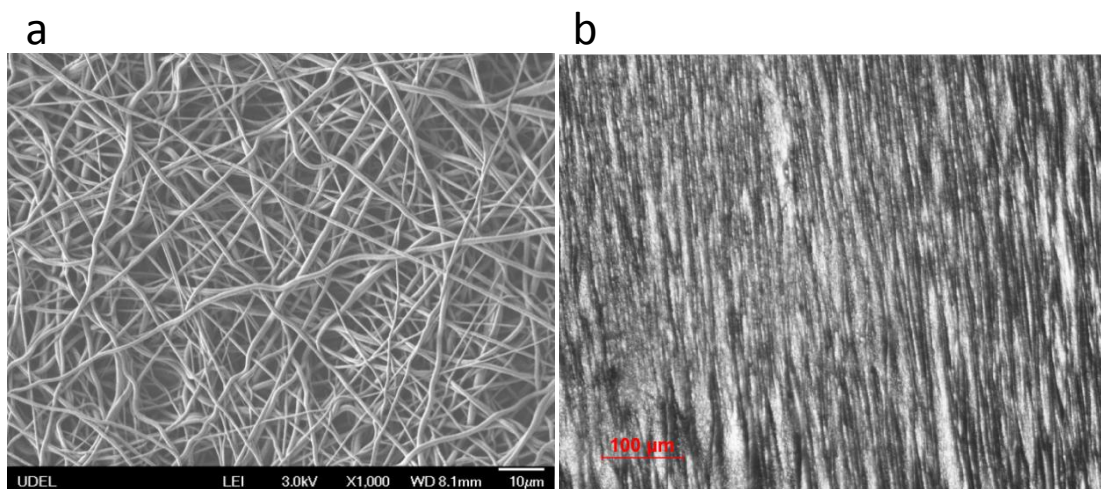


Figure 3.2 a) SEM image of the electrospun elastomeric separator. b) Optical image of the buckled SWNT film

1 mm thick PDMS substrate was used per SWNT electrode giving the whole device a thickness of approximately 2 mm. The whole device survived more than 5000

DSR cycles without fatigue-induced failure, demonstrating the excellent mechanical robustness. Fig. 3.2b shows the optical image of the buckled SWNT film, demonstrating uniform periodic wavy pattern, which is attributed to the strong bonding between the SWNT macrofilms and the PDMS substrates.

3.4.2 Electrochemical Behavior of DSS at static 0% Strain and 31.5% Strain

The electrochemical performance of the DSS was first evaluated using the CV measurement (from -1.5 to 1.5 V) in different scan rates from 50 mV s⁻¹ to 2000 mV s⁻¹. Fig. 3.3a displays the CV curves of the DSS at static 0 % and 31.5 % strain at scan rate of 2000 mV s⁻¹. With 13% more of the integral area of the CV loop, the specific capacitance of the DSS at 31.5% strain is 13 % higher than the cell at 0 % strain, according to the Equation (4.1):

$$C = \frac{A}{f \times v \times m} \quad (4.1)$$

where C is the specific capacitance, A is the integral area of the CV loops, f is the scan rate, v is the voltage window (3 V), and m is the mass of one SWNT electrode [26].

With a scan rate of 2000 mV s⁻¹ (charge and discharge in 1.5 s), the maximum current reached over than 10 mA, at a voltage of 1.5 V, which is suitable for practical applications, such as low power light-emitting diode (LED). The maximum current can be improved by increasing the electrode mass load, or by anchoring redox materials, such as MnO₂, using facile room temperature synthesis method [27].

For a scan rate of 50 mV s^{-1} , the CV curves at 0 % strain and 31.5 % strain are almost overlapped, as shown in Fig. 3.3b, with only 0.7 % higher of the calculated specific capacitance at 31.5% strain than at 0 % strain. The specific capacitance of the DSS under static strain at various scan rates is summarized in Fig. 3.3c. It shows that the specific capacitance of DSS gradually increased at both 0% strain and 31.5% strain with decreasing scan rate; however, the rate of increase is much higher for 0% strain compared to 31.5% strain. The reason could be attributed to the fact that with low scan rates, the charged ions have much longer time to be diffused into the inner Helmholtz layer to contribute to EDL. With high scan rates, there is not enough time for all the ions to move inside the inner Helmholtz layer, especially for the cell under 0 % strain, compared with the 31.5% strain.

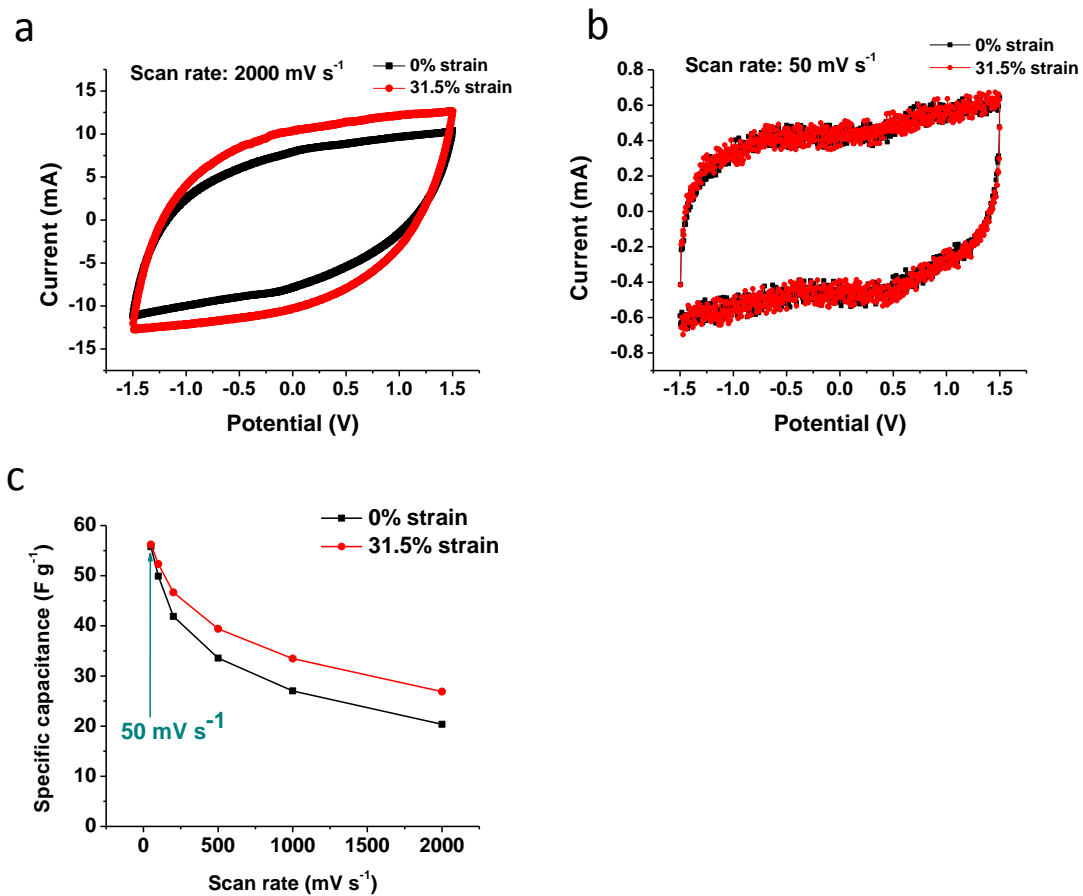


Figure 3.3 CV curves of DSS under static 0 % strain and 31.5 % strain at a) 2000 mV s^{-1} scan rate. b) 50 mV s^{-1} scan rate. c) summary of the specific capacitance vs. scan rates (from 50 mV s^{-1} to 2000 mV s^{-1})

3.4.3 Electrochemical Behavior of the DSS under DSR Mode

The electrochemical behavior of the DSS was further examined using the CV method under DSR mode, i.e. the cell is dynamic stretching and releasing between 0% strain and 31.5% strain at different strain rates, as illustrated in Fig. 3.4. For better comparison to see the strain rate effect, the scan rate of the CV test was kept same at 100 mV s^{-1} . For reference purpose, Fig. 3.4a shows the CV curve of the DSS at static 0% strain (black curve) and 31.5% strain (red curve). It shows that the red curve is larger than the black curve, resulting approximately 4 % difference of the specific capacitance at scan rate of 100 mV s^{-1} . The similar CV curve's changing caused by the different applied strain level was also reported [21]. However, there is no report on the cell under dynamic in situ applied strain. Comparatively, it is first time in our study to report the dynamic electrochemical behavior induced by the in situ applied DSR. From the above result, it is anticipated that the CV curve under DSR mode (blue curve) would shift between the CV curve of maximum strain (red curve) and CV curve of minimum strain (black curve), which is illustrated in schematic of Fig. 3.4b. It is also expected that the strain rate applied on the cell would affect the frequency of the changing CV curves under DSR mode.

Fig. 3.4c shows the CV curve of the DSS at a strain rate of $2.22\% \text{ strain s}^{-1}$, where the cell was stretched from 0 % strain to 31.5 % strain in 14.19 s. It can be seen that the electrochemical behavior of the cell is affected by the stretching and releasing as expected and illustrated in Fig. 3.4b. To elaborate, as the cell is stretched to

maximum strain, the green CV curve under DSR mode overlaps the red CV curve and as the cell is released to minimum strain, the green CV curve overlaps the black CV curve. After increasing the strain rate, the frequency of the changing CV curve is observed. Fig. 3.4d depicts the CV curve of the DSS at a higher strain rate of 4.46 % strain s^{-1} . At this strain rate, the DSS stretched from 0 % strain to 31.5 % strain in 7.06s. The figure shows that the CV curves are also constantly shifting, as expected. The only difference, compared to Fig. 3.4c, is that the frequency of shifting is increased approximately twice, owing to the doubled strain rate applied.

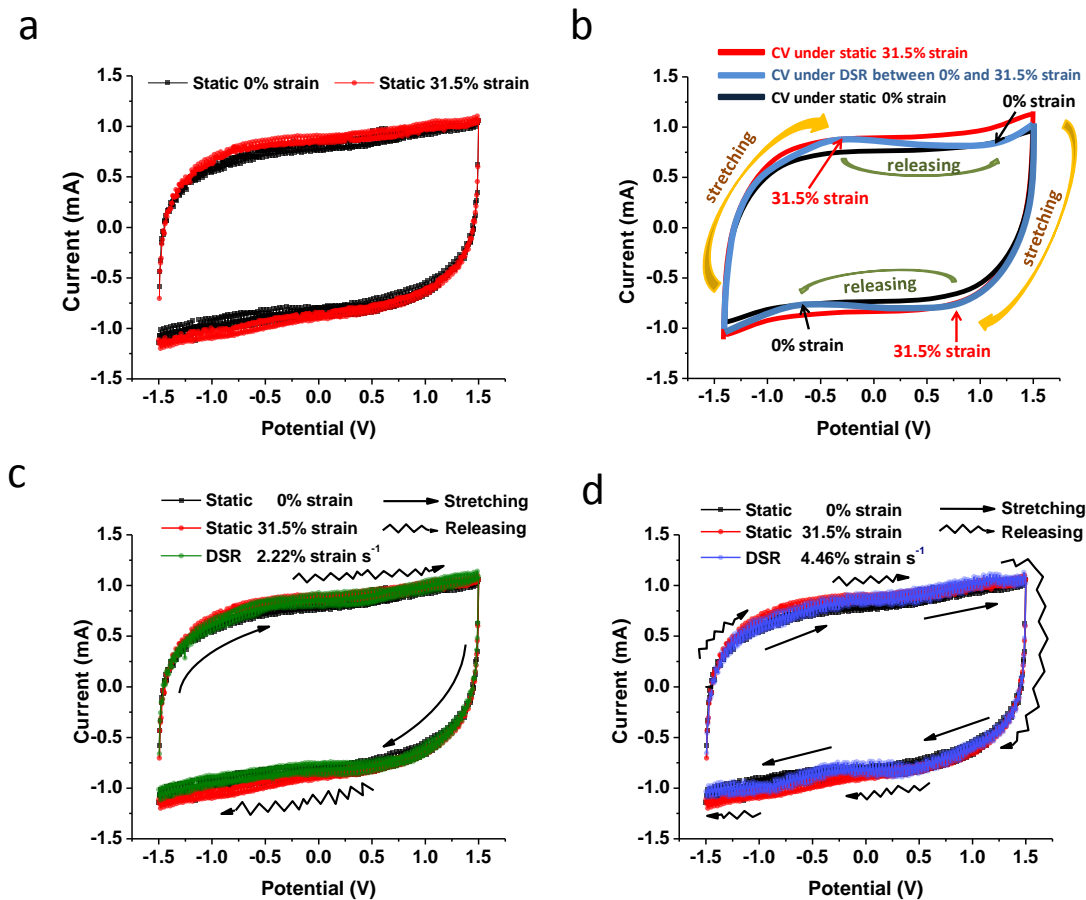


Figure 3.4 CV curves of DSS a) under fixed 0 % strain and 31.5 % strain. b) schematic of CV curve under DSR mode: gradually changes between CV curve at fixed 31.5% strain and fixed 0% strain. c) CV curves under dynamic stretching releasing (DSR) at 2.22% strain rate s⁻¹ d) at 4.46% strain rate s⁻¹ (Scan rate is 100 mV s⁻¹.)

In addition to the CV test, the galvanostatic charge/discharge experiment is performed at current density of 10 A g⁻¹, owing to the high power capability of the SWNT electrode. Fig. 3.5a shows the charge/discharge curve at strain rate of 4.46 % strain s⁻¹. The linear triangular shape of the charge/discharge curve confirms pure EDL behavior. The figure shows that it takes approximately 20 s for the cell to be charged

from -1.5V to 1.5V. It is worth to notice that, there is no significant affect from the physical *in situ* applied stretching/releasing of the cell (black curve) on the charge/discharge curve (red curve). The calculated specific capacitance is also relatively stable. It confirms again the mechanical robustness and the excellent electrochemical performance of the cell under extremely high strain rate applied.

In order to see the possible strain rate effect, the cell is also charged/discharged under 2.22 % strain s^{-1} and 1.11 % strain s^{-1} . Consistent with the CV behavior, it is observed that with small strain rate, the capacitance is in close relation to the strain rate applied, as illustrated in Fig. 3.5b,c. In order to clearly illustrate this phenomenon, the capacitance of the cell is normalized with the same standard of the current specific capacitance value of the cell divided by the initial specific capacitance value of the cell at 31.5% strain. It is discovered that the capacitance is fluctuated with relatively higher amplitude at strain rate of 2.22 % strain s^{-1} , and 1.11 % strain s^{-1} , compared to the cell at strain rate of 4.46 % strain s^{-1} . The reason could be attributed to the fact that, with smaller strain rate, the cell would be relatively stagnated at either highest strain point, or lowest strain point for longer period of time. In another word, the period of the DSS changing from 31.5% strain to 0% strain will be twice longer for the cell at strain rate of 1.11% strain s^{-1} , compared with 2.22 % strain s^{-1} . As a result, it is observed that at strain rate of 1.11 % strain s^{-1} , the cell tend to have the slowest period and much larger capacitance fluctuation. To better illustrate, the dynamic behavior of the cell under 3 different strain rates is enlarged and depicted in Fig. 3.5c. It clearly shows that the relatively stable performance of the cell at 4.46 % strain s^{-1} (blue curve)

than that of 2.22 % strain s^{-1} (green curve) and 1.11 % strain s^{-1} (yellow curve). The corresponding physical DSR is marked with the solid line (stretching) and dotted line (releasing) to show the coupling effect. Besides the fluctuation and frequency change under different strain rate, it is also very interesting to notice that, the averaged specific capacitance performance of the cell under 1.11 % strain s^{-1} , is slightly lower (approximately 1%) than that of 2.22 strain s^{-1} , and 4.46% strain s^{-1} , shown in Fig. 3.5c. The reason is explained in later section.

As important criteria to evaluate the cycling stability, the testing result of DSS under DSR mode is illustrated in Fig. 3.5d. Compared to literature reported[22], in which the cell was mechanically stretched for 100 times, then tested for the electrochemical cycling stability, the testing method under in situ DSR can more accurately reflect the real performance of the stretchable energy storage device. In this case, the capacitance retention is calculated from the current discharge specific capacitance, divided by the initial discharge specific capacitance value. The DSS achieved excellent cycling stability of 94.6% capacitance retention, with extremely high strain rate of 4.46% strain s^{-1} , after finishing total number of 2521 in situ stretching/releasing cycles. With lower strain rate applied, it is observed that the capacitance retention increased to 98.5 %, which could be attributed to smaller number of DSR cycles (677 cycles), with less possible fatigue-induced degradation of the cell.

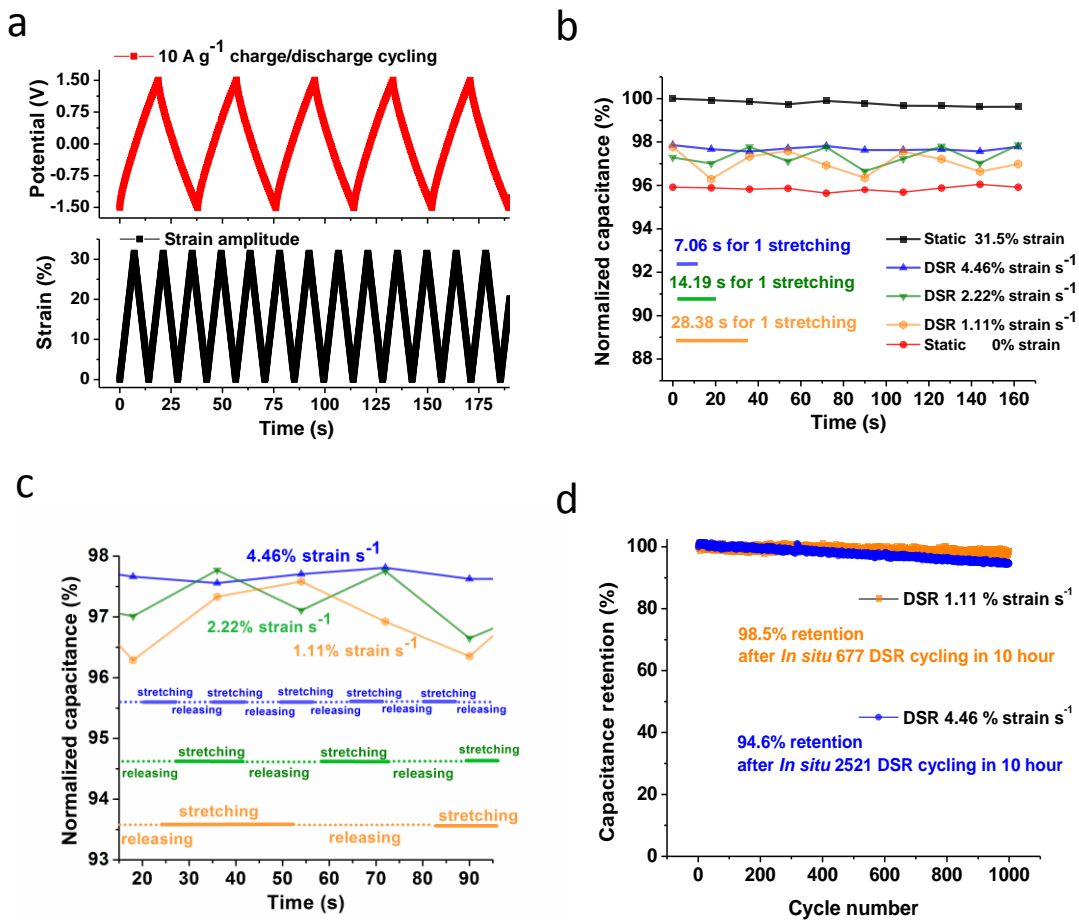


Figure 3.5 a) Galvanostatic charge/discharge curve at current density of 10 A g⁻¹, during *In situ* DSR at strain rate of 4.46 % strain s⁻¹ b) Comparison of the normalized capacitance (the capacitance divided by the initial capacitance value of the DSS fixed at static 31.5 % strain) with different strain rate. c) Enlarged figure to compare the specific capacitance of the cell under different strain rate applied. d) With *In situ* applied DSR cycling at high strain rate of 1.11 % s⁻¹ strain s⁻¹, and 4.46 % strain s⁻¹, the DSS shows good cycling stability. The current density is 10 A g⁻¹.

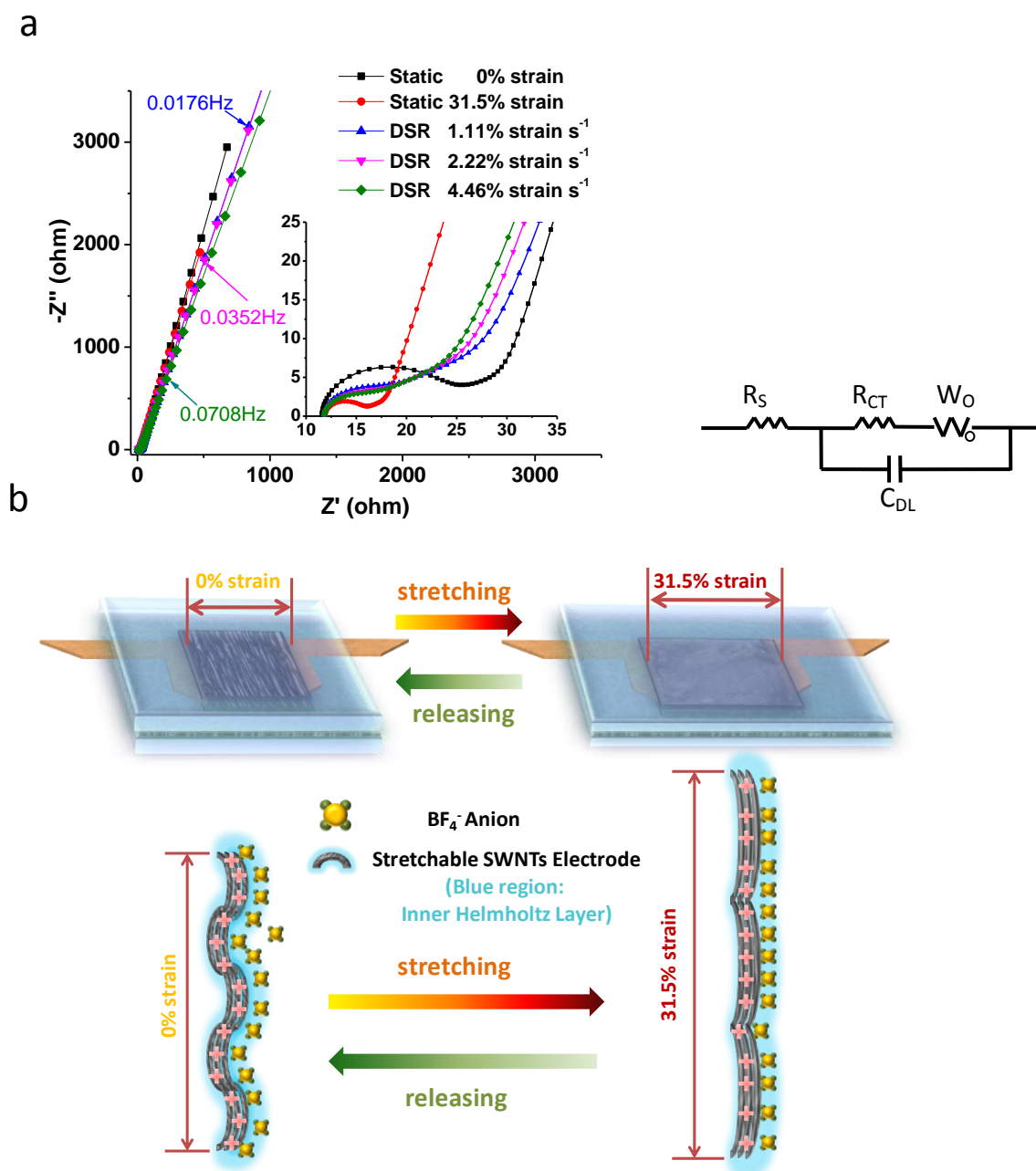


Figure 3.6 a) Nyquist plots of DSS at different strain and strain rate applied and the equivalent circuit in ZVIEW software (inset: high frequency region) b) Schematic of the DSS at different strain applied showing changing electrode/electrolyte interface due to stretching/releasing

Table 3.1 AC impedance equivalent circuit fitting parameters in ZVIEW

	R_S (Ω)	R_{CT} (Ω)	W_{oR} (Ω)	C_{DL} (μF)
0 % strain	11.6	11.38	19.34	9.55
31.5 % strain	11.9	3.38	7.74	10.22
DSR 1.11 % s ⁻¹	11.78	4.89	33.07	9.67
DSR 2.22 % s ⁻¹	11.85	3.97	30.65	9.81
DSR 4.46 % s ⁻¹	11.79	3.50	27.26	9.90

In order to understand the fundamental reason that affect the DSS on the capacitance behavior, the electrochemical impedance spectroscopy (EIS) was performed under static applied strain (0 % strain, 31.5% strain), as well as under DSR mode with different strain rate, as shown in the Nyquist plots of Fig. 3.6a. The AC impedance result was then fitted using Z view software with equivalent circuit to get the fitting parameters, shown in Table 3.1. As shown in Fig. 3.6a and Table 3.1, the series resistance (R_S) is not significantly altered due to the different strain or strain rate applied on the DSS. However, it is interesting to see that at static applied 31.5 % strain, the charge transfer resistance (R_{CT}) is significantly decreased (from 11.38 ohm at 0% strain to 3.38 ohm at 31.5% strain), indicating a much improved electrode/electrolyte interface compared to 0 % strain. The recent paper [21] also reported the similar phenomenon, induced by the applied strain, however did not provide more detailed explanation. The Warburg diffusion resistance (W_{oR}) is also decreased (from 19.34 ohm at 0% strain to 7.74 ohm at 31.5 % strain). Consequently, the double layer capacitance (C_{DL}) is larger at the maximum stretched state (31.5 % strain) , compared to original un-stretched state at 0% strain. As discussed previously, the different strain rate applied on the cell at DSR mode also slightly affected the

capacitance performance, although this difference (approximately 1 %) is almost negligible. The difference is found mainly contributed by the much increased Warburg diffusion resistance under DSR mode, compared to the static state of the stretchable cell. At Figure 3.6a, the AC frequency of the cell at different strain rate is also marked. At 1.11 % strain s^{-1} , based on the duration of the cell being stretched (28.38s) and released (another 28.38 s), the calculated frequency of the mechanical DSR cycling (stretched from 0 % strain to 31.5 % strain, then released back to 0 % strain) is equal to $1/56.76$ s, which is 0.0176 Hz (blue mark). Similarly at 2.22% strain s^{-1} and 4.46% strain s^{-1} , the corresponding frequency of the mechanical DSR cycling is 0.0352 Hz (pink mark) and 0.0708 Hz (green mark), respectively. It is easy to see that the corresponding ohmic element under those frequency is in the sequence of Z' (840 ohm at 1.11 % strain s^{-1}) > Z' (510 ohm at 2.22 % strain s^{-1}) > Z' (252 ohm at 4.46 % strain s^{-1}). In addition, as Table 1 shows, the Warburg diffusion resistance under the DSR mode is also in the sequence of W_{oR} at 1.11% strain > W_{oR} at 2.22% strain s^{-1} > W_{oR} at 4.46% strain s^{-1} .

Fig.3.6b presents a schematic of the microscale view of the electrode/electrolyte interface to explain the possible reason of the changing charge transfer resistance and Warburg diffusion resistance. At static 0 % strain, the buckled SWNT electrode formed period wavy structure on the macro scale. The resistance on the electrode/electrolyte interface is much higher. The ionic diffusion process is also hindered at this state, due to the relatively long ion migration and diffusion length to move inside the inner Helmholtz layer, compared to the state of cell at static 31.5 %

strain, when the pre-buckled SWNT electrode was stretched to be almost flattened. In other words, at 31.5 % strain, the flattened surface favors faster kinetics and more effective ion diffusion, thus increases the capacitance of the cell. Under the DSR mode, the diffusion element increase much, owing to the moving of the liquid electrolyte inside the cell during the stretching and releasing. At 4.46% strain s^{-1} , the charge transfer at the electrode/electrolyte interface and the diffusion process is slightly improved, compared to 2.22% strain s^{-1} and 1.11% strain s^{-1} , could be possibly contributed to the faster changing surface structure may favor the wavy electrode to keep more charged ions within the inner Helmholtz layer, and more portion of the charged ions within the effective outer diffuse layer (Couv-Chapman layer)[28]. However, this difference due to the DSR strain rate is found only in approximately 1 % range, thus for practical application, this difference would not affect significantly for the performance of the cell.

3.5 Conclusion

In this study, we reported the dynamic stretchable supercapacitor based on buckled SWNT macrofilms and elastomeric separator. The electrochemical behavior of this stretchable and rechargeable energy storage device has been systematically investigated under the dynamic stretching/releasing mode. The changing electrochemical behavior is analyzed with detailed explanation on changing charge/transfer resistance and Warburg diffusion resistance, both at static and DSR

mode. The DSS achieved excellent cycling stability under extremely high strain rate of 4.46% strain. The fabrication process is facile, scalable and cost-efficient for large scale industrial implementation. This successful demonstrated prototype DSS can be further optimized in terms of its energy and power density, and cycling stability, with optimized electrode and electrolyte combination, and sealing technique. Following the same concept, it is also possible to make the dynamic full stretchable rechargeable lithium-ion battery system to meet the high energy density applications, such as stretchable cell phones. With the future success combination of stretchable energy conversion materials, such as photovoltaic and piezoelectric materials, the fully self-supported stretchable power source device will be achieved for future self-powered and maintenance-free stretchable applications.

REFERENCES

- [1] D. H. Kim, J. A. Rogers, "*Stretchable electronics: materials strategies and devices*", *Advanced Materials*, vol. 20, pp. 4887-4892, 2008.
- [2] J.A. Rogers, T. Someya, Y. G. Huang, "*Materials and mechanics for stretchable electronics*", *Science*, vol. 327, pp. 1603-1607, 2010.
- [3] D. H. Kim, N. Lu, R. Ma, Y.S. Kim, R.H. Kim, S. Wang, J. Wu, S. M. Won, H. Tao, A. Islam, K. J. Yu, T. K. R. Chowdhury, M. Ying, L. Xu, M. Li, H.J. Chung, H. Keum, M. McCormick, P. Liu, Y.W. Zhang, F. G. Omenetto, Y. Huang, T. Coleman, J.A. Rogers, "*Epidermal electronics*", *Science*, vol. 333, pp.838-843, 2011.
- [4] T. Sekitani, H. Nakajima, H. Maeda, T. Fukushima, T. Aida, K. Hata, T. Someya, "*Stretchable active-matrix organic light-emitting diode display using printable elastic conductors*", *Nature Materials*, vol. 8, pp.494-499, 2009.
- [5] Z.B. Yu, X.F. Niu, Z.T. Liu, Q.B. Pei, "*Intrinsically stretchable polymer light-emitting devices using carbon nanotube-polymer composite electrodes*" *Advanced Materials*, vol. 23, pp. 3989-3994, 2011.
- [6] R.H. Kim, M.H. Bae, D. G. Kim, H. Cheng, B. H. Kim, D. H. Kim, M. Li, J. Wu, F. Du, H. S. Kim, S. Kim, D. Estrada, S. W. Hong, Y. Huang, E. Pop, J. A. Rogers, "*Stretchable, transparent graphene interconnects for arrays of microscale inorganic light emitting diodes on rubber substrates*" *Nano Letters*, vol. 11, pp. 3881-3886, 2011.
- [7] L. Xiao, Z. Chen, C. Feng, L. Liu, Z. Q. Bai, Y. Wang, L. Qian, Y.Y. Zhang, Q.Q. Li, K.L. Jiang, S. S. Fan, "*Flexible, stretchable, transparent carbon nanotube thin film loudspeakers*" *Nano Letters*, vol. 8, pp.4539-4545, 2008.
- [8] S.C.B. Mannsfeld, B.C.K. Tee, R.M. Stoltenberg, C.V. H.H. Chen, S. Barman, B.V.O. Muir, A.N. Sokolov, C. Reese, Z.N. Bao, "*Highly sensitive flexible pressure sensors with microstructured rubber dielectric layers*" *Nature Materials*, vol. 9, pp. 859-864, 2010.

- [9] T. Yamada, Y. Hayamizu, Y. Yamamoto, Y. Yomogida, A. Izadi-Najafabadi, D.N. Futaba, K. Hata, "A stretchable carbon nanotube strain sensor for human-motion detection" *Nature nanotechnology*, vol. 6, pp. 296-301, 2011.
- [10] D.J. Lipomi, M. Vosgueritchian, B.C-K. Tee, S.L. Hellstrom, J.A. Lee, C.H. Fox, Z.N. Bao, "Skin-like pressure and strain sensors based on transparent elastic films of carbon nanotubes" *Nature Nanotechnology*, vol. 6, pp.788-792, 2011.
- [11] C.J. Yu, Z.Y. Wang, H.Y. Yu, H.Q. Jiang, "A stretchable temperature sensor based on elastically buckled thin film devices on elastomeric substrates" *Applied Physics Letters*, vol. 95, pp.141912, 2009.
- [12] S. Cheng, Z.G. Wu, "Microfluidic stretchable RF electronics" *Lab On A Chip*, vol. 10, pp.3227-3234, 2010.
- [13] G. Shin, C.H. Yoon, M.Y. Bae, Y.C. Kim, S.K. Hong, J.A. Rogers, J.S. Ha, "Stretchable field-effect transistor array of suspended SnO₂ nanowires" *Small*, vol. 7, pp.1181-1185, 2011.
- [14] D.J. Lipomi, B.C.K. Tee, M. Vosgueritchian, Z.N. Bao, "Stretchable organic solar cells" *Advanced Materials*, vol. 23, pp. 1771-1775, 2011.
- [15] J. Lee, J.A. Wu, M.X. Shi, J. Yoon, S.I. Park, M. Li, Z.J. Liu, Y.G. Huang, J.A. Rogers, "Stretchable GaAs photovoltaics with designs that enable high areal coverage" *Advanced Materials*, vol. 23, pp.986-991, 2011.
- [16] Y. Qi, N.T. Jafferis, K. Lyons, C.M. Lee, H. Ahmad, M.C. McAlpine, "Piezoelectric ribbons printed onto rubber for flexible energy conversion" *Nano Letters*, vol. 10, pp. 524-528, 2010.
- [17] X. Chen, S.Y. Xu, N. Yao, S. Yong, "1.6 V nanogenerator for Mechanical Energy Harvesting Using PZT Nanofibers" *Nano Letters*, vol. 10, pp 2133-2137, 2010.
- [18] K.S. Kim, Y. Zhao, H. Jang, S.Y. Lee, J.M. Kim, K.S. Kim, J. H. Ahn, P. Kim, J.Y. Choi, B. H. Hong, "Large-scale pattern growth of graphene films for stretchable transparent electrodes" *Nature*, vol. 457, pp.706-710, 2009.
- [19] C.J. Yu, C. Masarapu, J.P. Rong, B.Q. Wei, H.Q.Jiang, "Stretchable supercapacitors based on buckled single-walled carbon-nanotube macrofilms" *Advanced Materials*, vol. 21, pp. 4793-4797, 2009.

- [20] C. Wang, W. Zheng, Z. Yue, C.O. Too, G. G. Wallace, "*Buckled, Stretchable Polypyrrole Electrodes for Battery Applications*" *Advanced Materials*, vol. 23, pp.3580-3584, 2011.
- [21] B.Yue, C. Wang, X. Ding, G. G. Wallace, "Polypyrrole coated nylon lycra fabric as stretchable electrode for supercapacitor applications", *Electrochimica Acta*, vol. 68, pp.18-24, 2012.
- [22] L.B. Hu, M. Pasta, F. La Manita, L.F. Cui, S. Jeong, H.D. Deshazer, J.W. Choi, S. M. Han, Y. Cui, "*Stretchable, porous, and conductive energy textiles*", *Nano Letters*, vol. 10, pp. 708-714, 2010.
- [23] M. Kaltenbrunner, G. Kettlgruber, C. Siket, R. Schwodiauer, S. Bauer, "*Arrays of ultracompliant electrochemical dry gel cells for stretchable electronics*", *Advanced Materials*, vol. 22, pp.2065-2067, 2010.
- [24] X. Wang, W. Wang, X. Li, B. Carlberg, X.Lu, Z. Cheng, J. Liu, S. Dongkai, "*Investigation of dielectric strength of electrospun nanofiber based thermal interface material*", *International symposium on high density packaging and microsystem integration*, pp. 1-6, 2007.
- [25] B. Carlberg, M. Z. Axell, U. Nannmark, J. Liu, H. G. Kuhn, "*Electrospun polyurethane scaffolds for proliferation and neuronal differentiation of human embryonic stem cells*", *Biomedical Materials*, vol. 4, pp.045004, 2009.
- [26] X. Li, J.P. Rong, B.Q. Wei, "*Electrochemical behavior of single-walled carbon nanotube supercapacitors under compressive stress*", *ACS Nano*, vol. 4, pp.6039-6049, 2010.
- [27] X. Li, B.Q. Wei, "*Facile synthesis and supercapacitive behavior of SWNT/MnO₂ hybrid films*", *Nano Energy*, published online March 16 2012.
- [28] B.E. Conway, "Electrochemical supercapacitors: scientific fundamentals and technological applications", pp.108-114. , Kluwer Academic/ Plenum Publishers, New York. 1999.

Chapter 4

FACILE SYNTHESIS AND SUPER CAPACITIVE BEHAVIOR OF SINGLE-WALLED CARBON NANOTUBE AND MANGANESE OXIDE HYBRID FILMS

4.1 Significance

In the previous two chapters, the freestanding SWNT film based flexible/stretchable supercapacitors are studied, which is suitable as power source for the lightweight flexible/stretchable electronics application. However, for large energy density demanding application, such as vehicles, or stationary application, flexible/stretchable properties would not be the critical feature. At that point, the energy density and power density would be much more important. As discussed previously, SWNT electrodes offer high power density, because of the excellent electrical conductivity, high frequency response [1]. It was reported [2] that SWNTs supercapacitor is capable of withstanding high current density of 100 A g^{-1} , yielding a high power density of 55 kW kg^{-1} . However, for the CNTs supercapacitor, the specific capacitance and energy density is still relatively poor, in the range of 40 F g^{-1} and 4 Wh kg^{-1} . Thus, it is very important to find a method to increase the energy density as well as keeping the excellent power density of the CNTs based supercapacitor. Thus, we investigated a facile method to improve the freestanding SWNT films based supercapacitor by anchoring redox materials to improve the performance.

4.2 Literature Review of Pseudocapacitive Materials

In order to improve the energy density, except using the organic electrolyte or ionic liquid with higher stabilized functional voltage, the most widely used method is to introduce the redox materials [3,4,5,6] which contribute on the specific capacitance, with fast and reversible faradaic surface reaction, as discussed previously.

Compared with conductive polymer (CPs) which typically suffer from swelling/shrinking during charge/discharge, transition metal oxides(TMOs) and transition metal hydroxides (TMHs) have a better stability, thus are more widely pursued.[7]There are a wide range of TMO materials, such as V_2O_5 [8], SnO[9], NiO[10], RuO_2 [11], CuO[12], MoO_3 [13]. Among the TMOs, RuO_2 has superior specific capacitance (SC) of 720 F g^{-1} , [14] but MnO_2 is more attractive owing to low cost, environmental friendliness and natural abundance.[15]

4.3 Introduction to SWNT/ MnO_2 Hybrid Film

In general, the low electrical conductivity of MnO_2 electrode material usually leads to low power performance. In order to improve the performance of MnO_2 electrode, CNTs are often used as a backbone for MnO_2 deposition, because of their high electrical conductivity, chemical stability and high mechanical strength. Many different approaches to synthesize CNT_s/ MnO_2 nanocomposites have been developed, such as physical mixing, [16] thermal decomposition,[17] hydrothermal method,[18]

and electrodeposition.[19] However, most of these routes are complicated and require long reaction time, limiting their industrial implementation. Therefore, it is of great interest to develop a facile and efficient method to synthesize nanostructure MnO₂ as electrode materials.

In a previous study, we used the precipitation method to reduce KMnO₄ with ethanol to synthesize MnO₂ and showed its excellent performance with SWNT composite in the aqueous electrolyte [20]. A similar approach was also demonstrated by Jiang et al.[21]. For the above electrode systems, however, one drawback is that inactive binder material and conductive carbon are still needed. Another drawback is that aqueous electrolytes only provide 1 V voltage window, limiting the energy density.

Here we report a new and facile approach to make SWNT/MnO₂ hybrid films, which is binder-free, robust, and with pre-formed electrical pathways. The approach has following merits: (i) facile synthesis with a short reaction time at room temperature, (ii) large voltage window by employing organic electrolyte, (iii) binder-free and no need to add electric conductor materials, and (iv) the industrial scalability. The entangled structure of SWNT films provides excellent electron path, significantly lowers the electrical resistivity of the nanostructured MnO₂, and improves the power density of the hybrid films. The SWNT/MnO₂ electrodes have the highest SC of 150 F g⁻¹, energy density of 70 Wh kg⁻¹, and power density of 79 kW kg⁻¹, with excellent cycling stability of 98.5% retention after 15,000 cycles at 50 A g⁻¹ and 1,000 cycles at 2 A g⁻¹, respectively.

4.4 Experimental Section

4.4.1 Preparation of SWNT/MnO₂ Hybrid Films Electrodes

First, the SWNT film is fabricated using the CVD method[22] introduced in Chapter 2. After that, the SWNT/MnO₂ hybrid film electrodes were prepared by modified simple precipitation.[23] Briefly, an SWNT film electrode on copper foil was immersed in ethanol, while 0.1 M KMnO₄ aqueous solution was added dropwise. A thin layer of nanostructured MnO₂ was deposited on the surface of the SWNT bundles in 30 min. The resulting SWNT/MnO₂ electrode was rinsed repeatedly in deionized water and ethanol and finally dried at room temperature for 24 h.

4.4.2 Structural Characterization and MnO₂ Loading Measurement

Transmission electron microscopy (TEM) and scanning electron microscopy (SEM) images were taken with a JEOL JEM-2010F microscope and a JEOL JSM-7400F microscope, respectively. In order to ensure the accuracy of the MnO₂ loading measured, a Mettler Toledo microbalance XP6 with 0.001 mg readability was used. The weight was measured following the standard procedure: 3 copper foils punched from the same piece foils for SWNT coating were measured to get the average weight of copper foil substrates; the copper foils coated with SWNT films were punched and weighted; after MnO₂ reaction coating, the SWNT/MnO₂ composite electrodes were weighted to calculate the mass of the precipitated MnO₂. The weight difference of

SWNT electrode before and after coating MnO_2 shows average 20 wt.% mass loading of MnO_2 precipitated on the surface of SWNT bundles.

4.4.3 Electrochemical Measurements

Electrochemical measurements were carried out using symmetric coin cells, for both SWNT/ MnO_2 supercapacitors and SWNT supercapacitors (control samples). A 1 M tetraethylammonium tetrafluoroborate (TEABF_4) (Alfa Aesar) dissolved in battery-graded propylene carbonate (PC) (Alfa Aesar) solvent was used as the organic electrolyte. A Wattman glass microfiber paper was used as the separator. The supercapacitors were assembled in an Argon-filled Unilab glove-box. The cyclic voltammograms were performed with an EG&G PARSTAT 2273 potentiostat/galvanostat with various scan rates. The electrochemical impedance spectroscopy (EIS) was conducted at frequency range from 100 kHz to 10 mHz. The EIS data fitting program ZVIEW was used to obtain the equivalent circuit parameters. The galvanostatic charge-discharge measurements were performed on an Arbin BT4+ test system. All electrochemical measurements were performed at room temperature.

4.5 Results and Discussion

4.5.1 Reaction Mechanism to Synthesize SWNT/MnO₂ Hybrid Films

Fig. 4.1 depicts the precipitation process of MnO₂ on a punched SWNT film electrode. In this process, hydrophilic functional groups[22] on the surface of the SWNT bundles act as nucleation sites for MnO₂ anchoring. During about 30 min synthesis, brown precipitates were deposited onto the SWNT film, while purple color of the solution gradually disappeared. In this reaction, CH₃CH₂OH is oxidized into CH₃COOH and MnO₄⁻ is reduced into MnO₂ with the formation of KOH, then KOH is neutralized by CH₃COOH, to form CH₃COOK and H₂O.[23, 24]

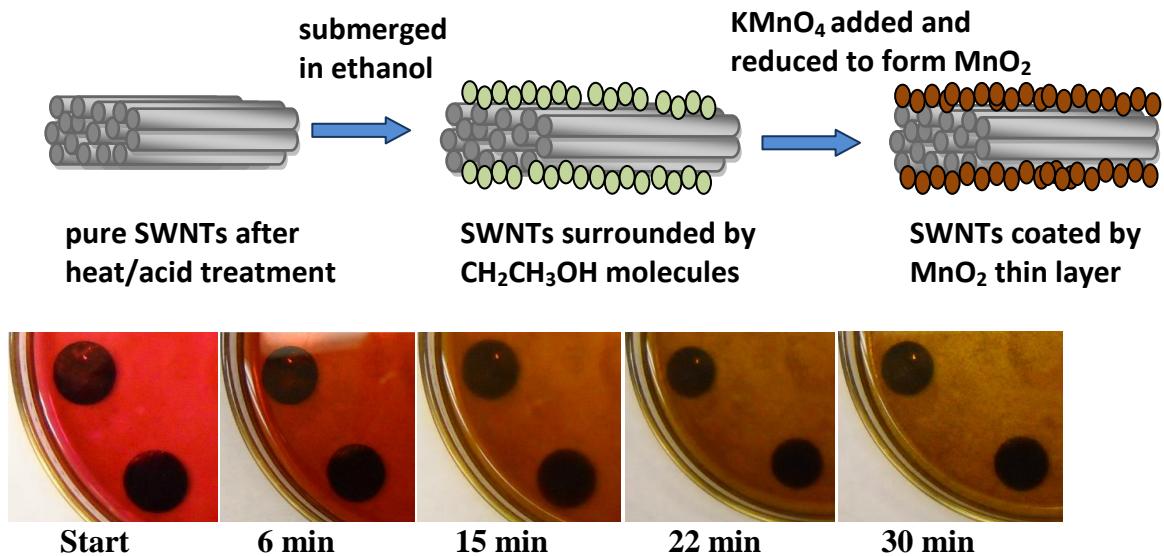


Figure 4.1 Schematic illustration of the synthesis process of nano-MnO₂ on the surface of SWNTs macro-film and the corresponding snapshots of the process taken with a camera.

Fig. 4.2a presents the typical SEM image of the pristine SWNT films. It can be seen that the SWNT bundles are entangled and interconnected with a combination of mesoporous and macroporous structures, providing excellent electrical conductivity. Fig. 4.2b illustrates the morphology of the SWNT/MnO₂ hybrid films. The MnO₂ nanoparticles uniformly deposited on the surfaces of the SWNT bundles. Since the spontaneously coated layer is not perfectly smooth, it could provide a larger surface area for better electrode/electrolyte interfacial contact. After long charge/discharge cycling (15,000 cycles) in 1M TEABF₄/PC electrolyte, the coin cell supercapacitor was disassembled to examine the surface morphology of the cycled SWNT/MnO₂ electrode (Fig. 4.2c). Compared to Fig. 4.2b, it seems that the SWNT/MnO₂ are aggregated after cycling, which is actually caused by un-removed residues from the electrolyte salts, confirmed by X-ray energy dispersive spectroscopy (XEDS). Except the electrolyte residues observed, the MnO₂ thin layer remains the similar morphology after the long cycling, indicating a strong bonding between SWNT and MnO₂.

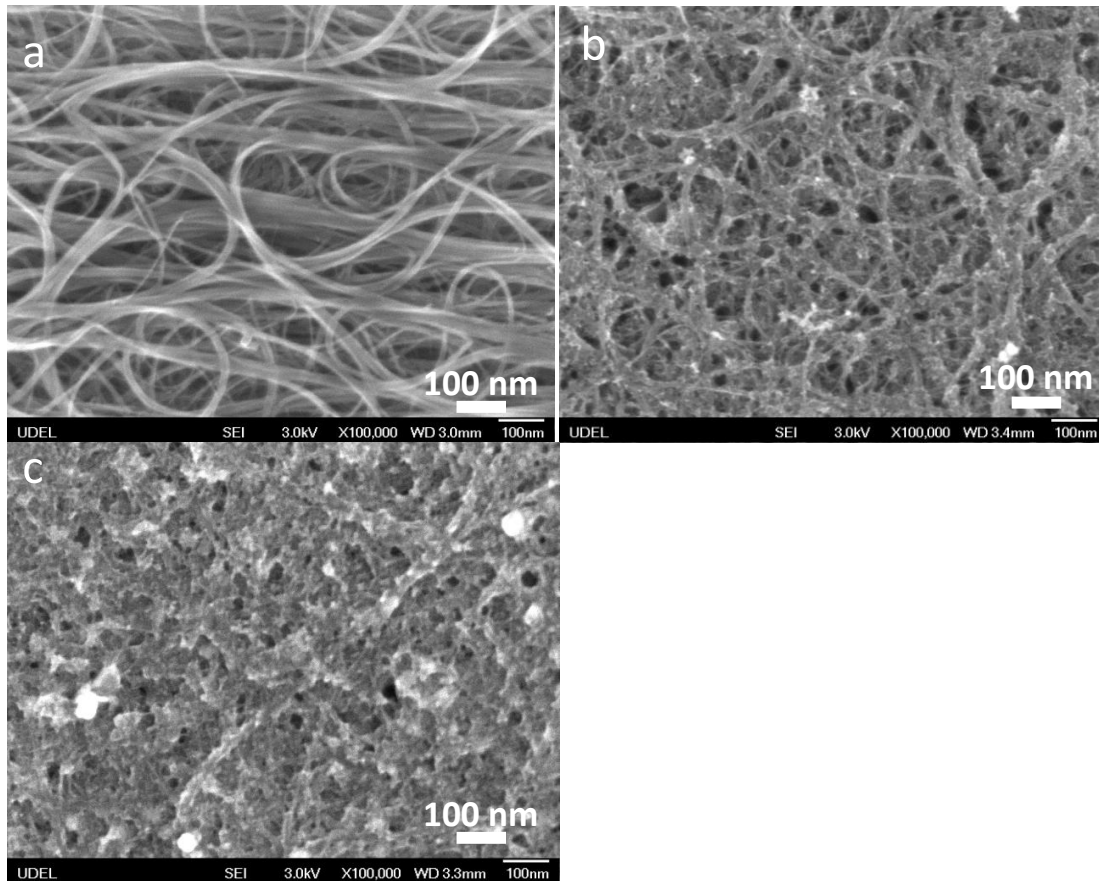
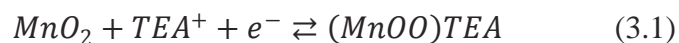


Figure 4.2 SEM images of a) SWNT film as synthesized before coating MnO_2 layer. b) SWNT/ MnO_2 electrode material as-synthesized. c) SWNT/ MnO_2 electrode material after 15,000th cycles.

4.5.2 Electrochemical Behavior of the SWNT/MnO₂ Hybrid Films

The electrochemical performances of the SWNT/MnO₂ and SWNT electrodes (control samples) in 1 M TEABF₄/PC electrolyte were evaluated using the cyclic voltammograms (CVs), with a wide potential window from -1.5 to 1.5V. Fig. 4.3a displays the CV curves of SWNT/MnO₂ electrode with various scan rates (from 50 to 2,000 mV s⁻¹), with the current response normalized with respect to the electrode mass. It shows that with a higher scan rate of 2000 mV s⁻¹, the normalized current is higher than that of 200 mV s⁻¹. This can be understood that the charging process takes shorter time (i.e. 1.5 s at 2000 mV s⁻¹ scan rate to increase from -1.5 V to 1.5 V, compared with 15 s for 200 mV s⁻¹ to increase from -1.5 V to 1.5 V.) for enough amount of ions to be attracted to the two electrodes to build the same potential. Fig. 4.3b presents the CV curve comparison of the SWNT/MnO₂ electrode and the SWNT electrode at the scan rate of 500 mV s⁻¹. It shows the normalized current increased dramatically for the SWNT/MnO₂ electrode, owing to the redox reaction of MnO₂. Compared with the SWNT electrode (black curves), a slight distortion is observed for the SWNT/MnO₂ electrode, which is attributed to the relatively high resistance of the coated nano-MnO₂ and relatively low conductivity of the 1M TEABF₄/PC organic electrolyte (13 mS cm⁻¹)[25]. The SWNT/MnO₂ electrode has redox peak from 0.6 to 1.2V. The intercalation/deintercalation of the tetraethylammoniumcation(TEA⁺) from TEABF₄/PC electrolyte leads to the reversible redox transition of Mn⁴⁺ from/to Mn³⁺, which can be described as Equation (3.1):



In order to further ensure the strong bonding and the anchoring stability of the MnO₂ nanoparticles on SWNTs, TEM images were recorded before and after the long charge/discharge cycling (Fig. 4.3c and Fig. 4.3d). Lattice structures can clearly be seen in the SWNT/MnO₂ hybrids, showing the polycrystalline feature of MnO₂ (marked with red square), both in as-synthesized SWNT/MnO₂ electrode and the electrode after long charge/discharge cycling. The ultra-thin MnO₂ layer (approximately 3 nm) is loaded on SWNT bundles and the stability of the MnO₂ layer is not affected by the electrochemical testing. The merit of the ultra-thin layer of the MnO₂ grown on SWNT bundles is that it greatly shortens the diffusion paths of the electrolyte ions during the fast charge/discharge process, and ensures the high utilization of the MnO₂ nanoparticles, contributed by the surface pseudocapacitive reaction of MnO₂. [26]

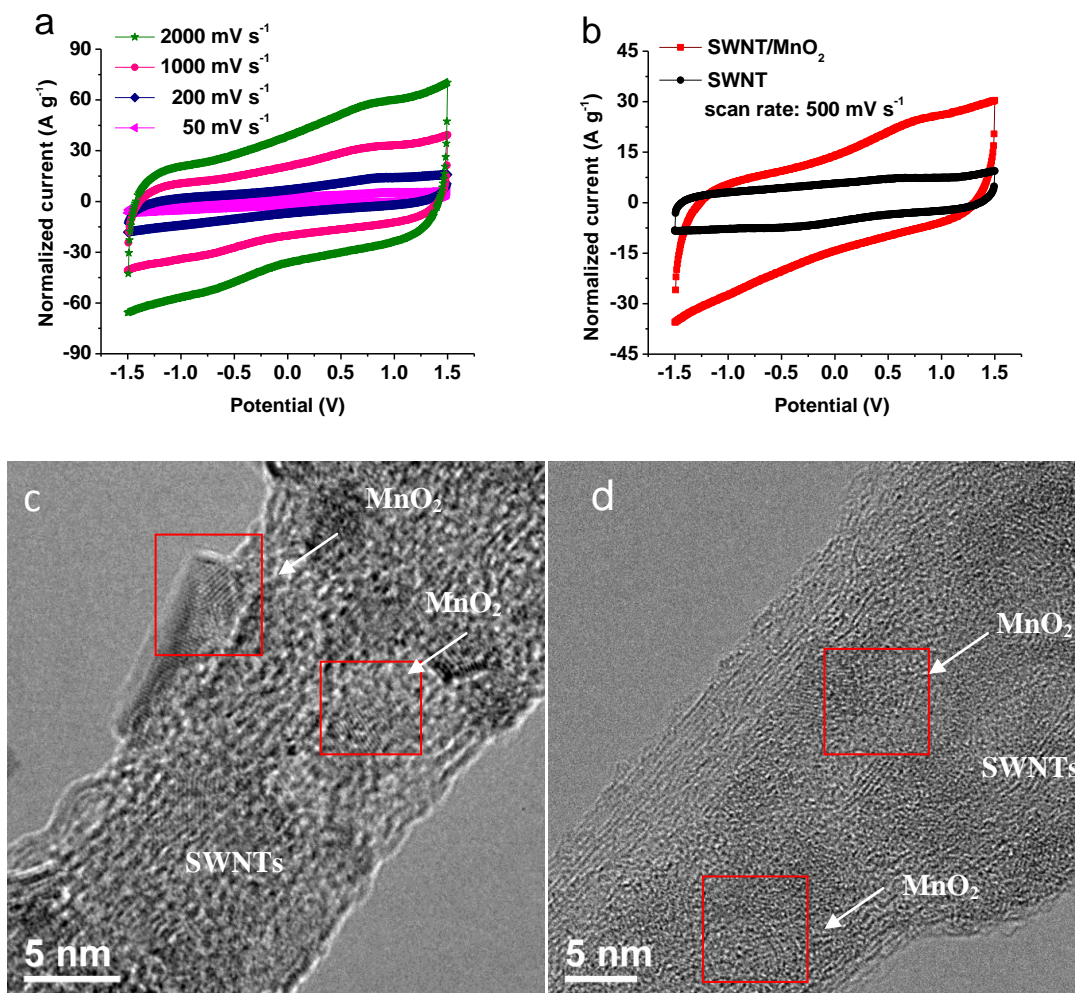


Figure 4.3 a) CV curves of SWNT/MnO₂ electrode measured at different scan rates (50 mV s⁻¹ to 2,000 mV s⁻¹). b) Comparative CV curves of SWNT/MnO₂ and SWNT at scan rate of 500 mV s⁻¹. c) TEM image of SWNT/MnO₂ electrode material before cycling. d) TEM image of SWNT/MnO₂ electrode material after the 15,000th cycles cycling.

The specific capacitances of the electrodes are summarized in Fig. 4.4a, according to Equation (3.2):

$$C_s = \frac{A}{SR \times V \times M} \quad (3.2)$$

where C_s , A , SR , V , and M denote the SC, the integral areas of the cyclic voltammogram loops, the scan rate, the potential window, and the mass of electrodes, respectively. The SCs of SWNT/MnO₂ (based on total mass of the electrode, and based on mass of MnO₂) and SWNT electrode are plotted as a function of scan rates (from 2 to 2,000 mV s⁻¹).

It should be pointed out that, the total weight of the SWNT/MnO₂ electrode is contributed by approximately 80% of the SWNT film and 20% of loaded MnO₂. In order to estimate the SC based on MnO₂, the capacitance contribution of SWNT from total capacitance of SWNT/MnO₂ composite is deducted using the Equation (3.3):[27]

$$C_{s-Mn} = \frac{C_{s-com} - C_{s-NT} \times (1-20\%)}{20\%} \quad (3.3)$$

where C_{s-Mn} is the SC based on MnO₂ (blue line in Fig. 4.4a); C_{s-com} is the SC based on SWNT/MnO₂ hybrid film electrode, and C_{s-NT} is the SC based on the SWNT films, respectively.

In order to better illustrate the SWNT/MnO₂ electrode performance, the black curve in Fig. 4.4a shows the specific capacitance of the pure SWNT film electrodes (as the control sample), which is insensitive to the scan rate compared to the SWNT/MnO₂ electrodes. This is because of the rapid formation of the double layers in the pure SWNT film electrodes. For SWNT/MnO₂ electrodes, a dramatic increase of

the specific capacitance is observed at small scan rates below 10 mV s^{-1} , indicating a strong scan rate dependence of the specific capacitance. The increase of the specific capacitance is largely contributed from the redox reaction which would take a relatively longer time, compared to the pure electrical double layer formation within the pure SWNT electrodes. It should be noted however, at a fast scan rate above 500 mV s^{-1} , the specific capacitance of SWNT/MnO₂ electrode still outperforms the SWNT electrode, showing excellent rate capability owing to the pre-formed fast electron path in the SWNT network.

At 2 mV s^{-1} scan rate, the SC based on the total mass of SWNT/MnO₂ is 151 F g^{-1} , and the SC of the MnO₂ in the SWNT/MnO₂ hybrid films is evaluated as high as 596 F g^{-1} . Compared to the theoretical SC of MnO₂ (1370 F g^{-1}), the degree of electrochemical utilization is $\sim 44\%$ for MnO₂ in the SWNT/MnO₂ electrode. The reason of such high SC of MnO₂ is probably owing to the deeper diffusion of electrolyte ions into the thin MnO₂ layer to contribute to redox reaction. While at a high scan rate of $2,000 \text{ mV s}^{-1}$, the SC based on the total mass of SWNT/MnO₂ electrode is 38 F g^{-1} , and the SC based on the mass of MnO₂ is 109 F g^{-1} , indicating a low capacitance contribution from MnO₂ (less than 10%). The relatively decreased value of SC is attributed to the intrinsic low conductivity of the MnO₂ layer.

Ragone plot in Fig. 4.4b exhibits the high energy and power density feature of the SWNT/MnO₂ electrode. Consistent with the SC plots, the SWNT/MnO₂ electrodes delivered a much higher energy density while keeping equally high power density, compared with the SWNT electrodes in TEABF₄/PC electrolyte. To be

specific, at current density of 100 A g^{-1} , the SWNT/MnO₂ based supercapacitor delivered an energy density of 6.2 Wh kg^{-1} at an extremely high power density of 79 kW kg^{-1} , in contrast with the 3.6 Wh kg^{-1} at the power density of 82 kW kg^{-1} of the SWNT electrode. The slight decrease (3%) of the power density of SWNT/MnO₂ electrode could be attributed to the longer electrolyte ion diffusion paths caused by the thin MnO₂ layer. However, compared with the 72% increase of the energy density, the decrease of 3% power density becomes negligible, because of the presence of the highly-conductive SWNT film that facilitates the kinetics of electron transport path. At this ultra high current density, the SWNT/MnO₂ electrode finishes one cycle within one second, indicating excellent power capability. At a small current density (0.1 A g^{-1} , one full cycle takes approximately 4 hours in total), the energy density of the SWNT/MnO₂ electrode reached 70 Wh kg^{-1} at the power density of 77.3 W kg^{-1} , providing seven times higher energy density at the same power density, compared to the SWNT electrode (10 Wh kg^{-1} at the power density of 77.7 W kg^{-1}).

It should be noted that the energy density of the present SWNT/MnO₂ electrode outperformed the Ni-MH rechargeable battery, [28] which is highlighted in green belt part of Fig. 4.4b, although it is not competitive with the Li-ion battery indicated in orange belt part. At 1 A g^{-1} current rate, the cell performs one full charge in approximately 180 s, which is 20 C rate in terms of the current rate for an Li-ion battery during charging/discharging. At this high current rate, the SWNT/MnO₂ electrode provides power density of 0.8 kW kg^{-1} , and energy density of 20 Wh kg^{-1} , which is very competitive to the performance of Li-ion batteries. In addition, 20 C

current rate is extremely detrimental to the cycling stability of Li-ion batteries. So for high power and relatively low energy density applications, the SWNT/MnO₂ electrode is a very promising alternative to complement the current Li-ion battery systems. At a high energy density over 30 Wh kg⁻¹, however, lithium batteries have a higher power density than the SWNT/MnO₂ electrode, probably because the faster Li-ion intercalation/extraction contributed by the smaller ion size of Li⁺, compared to the slower redox reaction limited by the larger ion size of TEA⁺.

Fig. 4.4c presents the galvanostatic charge/discharge curves of SWNT/MnO₂ electrode at various current densities. It should be noted that the slightly asymmetric charge/discharge curves for the current densities below 20 A g⁻¹ is due to contribution from the pseudocapacitance of MnO₂ because a redox reaction typically takes more time than pure EDL formation. The small IR drops [20] are observed at the high charge current densities, which decrease with lowering the current density, as marked in Fig. 4.4c.

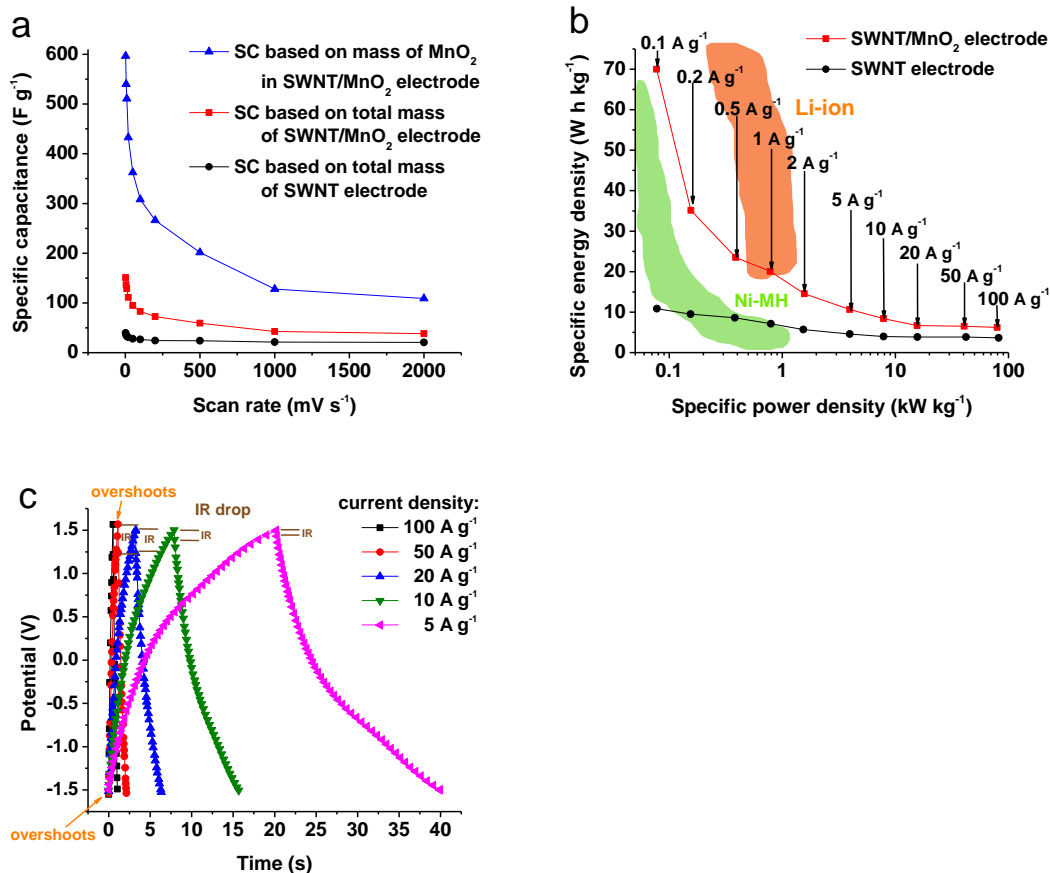


Figure 4.4 a) Comparison of specific capacitances of SWNT/ MnO_2 electrode (blue line: based on mass of MnO_2 ; red line: based on total mass of SWNT/ MnO_2) and SWNT electrode at different scan rates. b) Ragone plots of SWNT/ MnO_2 electrode and SWNT electrode at different current densities ($0.1 A g^{-1}$ to $100 A g^{-1}$). Green and orange transparent regions indicate the Ragone plot of Ni-MH and Li-ion batteries extracted from ref. [28]. c) Galvanostatic charge/discharge curves of SWNT/ MnO_2 at different current densities ($5 A g^{-1}$ to $100 A g^{-1}$)

In addition to the high energy and power density, the SWNT/MnO₂ hybrid films exhibited excellent long cycle stability. We performed the cycling test for 15,000 cycles at current density of 50 A g⁻¹ (Fig. 4.5a), and for 1,000 cycles at 2 A g⁻¹ (Fig. 4.5b), respectively. At the current density of 50 A g⁻¹, one charge-discharge cycle finishes in 2 seconds. The SC of both the SWNT/MnO₂ electrode and the SWNT electrode slightly increased and then stabilized at around the 3,000th cycle. This is attributed to more accessible porous surfaces to the electrolyte ions after numbers of cycles. Thus, the effective surface area increased and the capacitance improved.

It should be noted that the SC fluctuation is attributed to the overshoots,^[29] observed at the higher current density of 50 A g⁻¹, contributing to the variation of the SC (41 ± 3 F g⁻¹). However, the overshoots do not degrade the stability of the cells, because of the high operation window of 2.5 V for TEABF₄/PC electrolyte.[25]

The overshoots are avoided for the SWNT/MnO₂ electrode at a small current density of 2 A g⁻¹, resulting in high and narrow columbic efficiency (98.5% to 99%). The SC is very stable in the range from 118 to 121 F g⁻¹, 3 times of that for the SWNT electrode (38.6 to 40 F g⁻¹), providing a much higher capacitance and remaining an excellent cycling stability. Fig. 4.5c shows a randomly-picked, continuous 6 charge-discharge cycle profile, which exhibits very good stability of the SWNT/MnO₂ electrode.

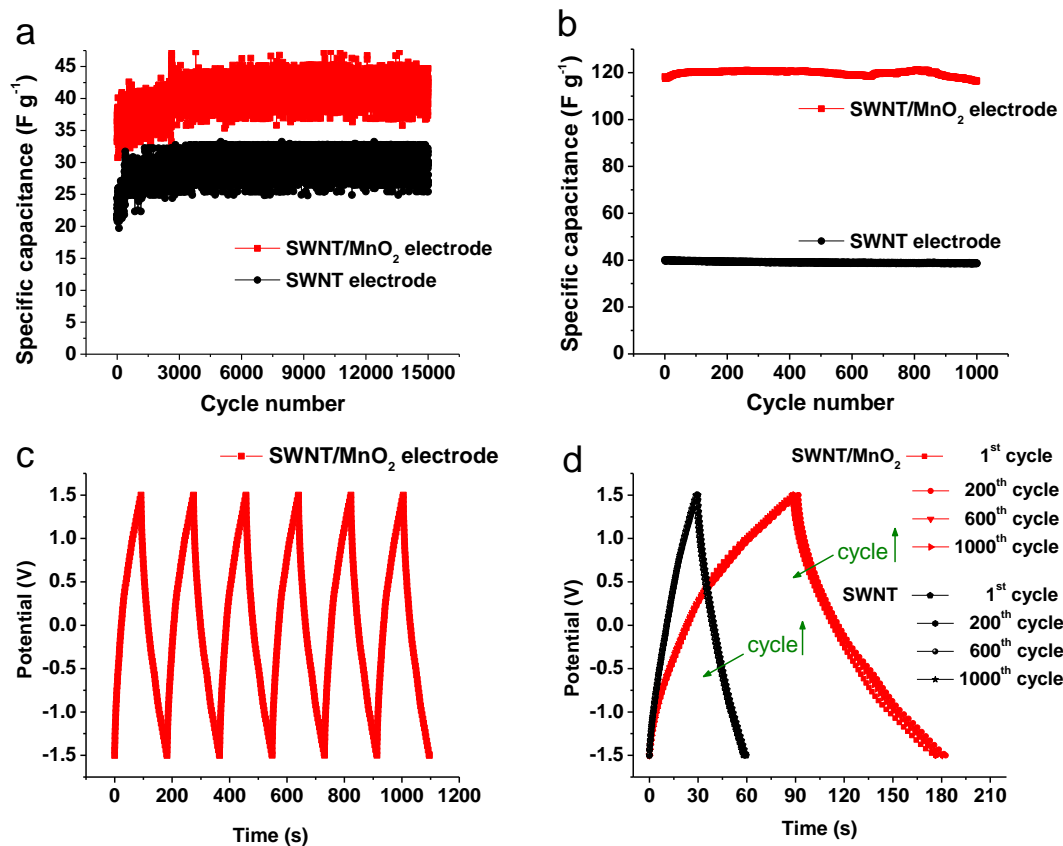


Figure 4.5 Cycle performance comparison of SWNT/MnO₂ electrode and SWNT electrode in TEABF₄/PC electrolyte. a) 15,000 cycles at current density of 50 A g⁻¹. b) 1,000 cycles at current density of 2 A g⁻¹. c) Randomly-picked continuous 6 charge-discharge cycle profile of SWNT/MnO₂ electrode at current density of 2 A g⁻¹. d) Galvanostatic charge/discharge curves from the 1st to the 1,000th cycles for SWNT/MnO₂ and SWNT electrode at 2 A g⁻¹ (arrow indicates the direction where cycle number is increasing).

To better illustrate the stability and comparison, charge-discharge curves of the SWNT/MnO₂ and the SWNT electrode are given in Fig. 4.5d at the current density of

2 A g⁻¹. The charge-discharge profiles of the SWNT/MnO₂ electrode exhibited a slightly distorted triangular symmetry, indicating pseudocapacitive behavior, as discussed above. The SWNT electrode exhibited almost a linear curve, suggesting an ideal EDLC behavior. Compared with the SWNT electrode, both charge and discharge time increased to 3 times for the SWNT/MnO₂ electrode, consistent with the increased energy density. From the 1st to the 1,000th cycles, the charge discharge curves at different cycle numbers almost overlap with each other, for both the SWNT/MnO₂ and the SWNT electrodes, which prove excellent cycling stability. The IR drops of both electrodes are from 1.5 V to 1.44 V at the initial cycle, and there is no significant difference after long cycles (At 100th cycle, both IR drops are from 1.5 V to 1.42 V). This also indicates the good stability, compared with previous research.[20, 24]

In order to evaluate the frequency response of the SWNT/MnO₂ and SWNT electrodes and better understand the possible change of these two different electrodes before and after long cycling, EIS was performed in the frequency range of 100 kHz – 0.1 Hz at open circuit potential (Fig. 4.6).

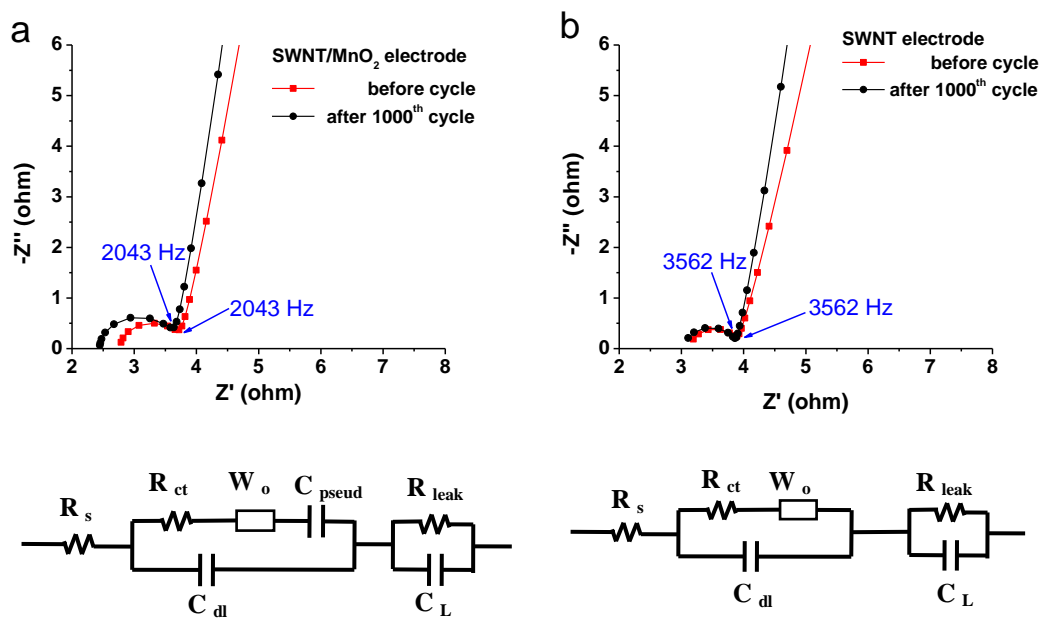


Figure 4.6 Nyquist plots of a) SWNT/MnO₂ and b) SWNT electrode before and after 1,000 cycles with the electrical equivalent circuits used for fitting impedance spectra.

Two different equivalent circuit models were used to simulate the capacitive and resistive elements of the two cells. For the SWNT electrode, the elements in the equivalent circuit include the series resistance (R_s), the double-layer capacitance (C_{dl}), the charge transfer resistance (R_{ct}), the Warburg diffusion element (W_o), the leakage resistance (R_{leak}), and the mass capacitance (C_L). [29] For the SWNT/MnO₂ electrode, the pseudocapacitance element (C_{pseud}) is associated with the redox capacitance. The curve fitting values are summarized in Table 4.3.

Table 4.1 Impedance curve fitting results of the SWNT/MnO₂ and the SWNT electrodes, before and after long cycling, in TEABF₄/PC using ZVIEW.

SWNT	R _s (Ω)	R _{ct} (Ω)	W _{oR} (Ω)	C _{dl} (μF)		R _{leak} (kΩ)	C _L (mF)
Before cycle	3.13	0.75	1100	7.95		19.98	1.30
After cycle	3.06	0.83	734	7.11		19.30	1.30
SWNT/MnO ₂	R _s (Ω)	R _{ct} (Ω)	W _{oR} (Ω)	C _{pseud} (μF)	C _{dl} (μF)	R _{leak} (kΩ)	C _L (mF)
Before cycle	2.71	0.97	7322	1500	12.6	0.61	3.80
After cycle	2.48	1.24	4027	2500	24.7	0.63	10.50

Theoretically, the Nyquist plot for supercapacitor consists of a high-frequency semicircle arc and a low-frequency straight line. The high-frequency semicircle is corresponding to R_{ct} at the electrode/electrolyte interface, and the low-frequency straight line is corresponding to ion diffusion in the electrode material. R_s is determined by the first intersection point on the real axis of the Nyquist spectrum in the high-frequency region, which is mainly contributed from the electrolyte resistance, the ionic resistance of ions moving through the separator, the intrinsic resistance of the active electrode material, and the contact resistance at the interface of active material/current collector. R_{ct} shown as the second intersection point of the semicircle on the real axis is mainly contributed by the resistance at the electrode/electrolyte interface. [5] As shown in Fig. 4.6, the low frequency straight line is almost vertical, indicating a good capacitive behavior. With SWNT films acting as pre-formed electric pathways, the R_s of SWNT/MnO₂ electrode is similar to that of the SWNT electrode, with slightly higher R_{ct} than SWNT electrode due to the redox reactions. Both

SWNT/MnO₂ electrode and SWNT electrode have very small arc region, indicating a good conductivity of the active materials and current collector. For comparison, we also measured the MnO₂ directly deposited on the current collector (copper substrate), which exhibited a much higher series resistance and charge-transfer resistance (20 Ω), due to the poor electrical conductivity of the MnO₂ cell.

To characterize the frequency response, the knee frequency is usually examined, representing the maximum frequency the energy stored can fully access.[30] In this work, the knee frequency is as high as 3,562 Hz and 2,043Hz, for the SWNT electrode and the SWNT/MnO₂ electrode, respectively. This ultra-high knee frequency indicates superior frequency response, compared with literature. [5, 31-33]

As shown in Table 4.1, the value of R_s slightly decreased after cycling for both the SWNT electrode and the SWNT/MnO₂ electrode, believably owing to an improved wetting of the separator and electrode/electrolyte interfaces. The R_{ct} of both SWNT/MnO₂ and SWNT electrodes increased slightly after long cycling, which could be attributed to the corrosion of the current collector by the dissolved oxygen in electrolytes during the cycling.[34] The similar phenomenon of increasing R_{ct} after long cycling was also observed by other groups.[34,35] Compared with the recently reported Graphene/MnO₂ composite,[34] which showed significantly increased R_{ct} (from 1.7 to 4.2 Ω), the increment in the current experimental results is much lower (from 0.97 to 1.24 Ω), in consistent with the excellent stability of the SWNT/MnO₂. The Warburg diffusion element after long cycling is decreased due to the easier accessibility of the electrolyte into the electrode materials for both SWNT and

SWNT/MnO₂, where SWNT/MnO₂ has a higher Warburg diffusion resistance due to the thin MnO₂ layer. Compared with the SWNT, the SWNT/MnO₂ electrode has two components to contribute to the capacitance, C_{dl} and C_{pseud}. The fitting values show that the pseudocapacitance contributes in a much higher ratio than the double layer capacitance. It is interesting to notice that both C_{dl} and C_{pseud} increased after cycling, probably owing to the increasing functional porous area and/or better wetting of the electrolyte/electrode interfaces.

4.6 Conclusions

In summary, we have successfully fabricated binder-free SWNT/MnO₂ hybrid films as supercapacitor electrodes using a facile precipitation method. The performance of the SWNT/MnO₂ electrodes in 1M TEABF₄/PC organic electrolyte demonstrates a much improved energy density and equally high power density, as well as an ultra-high frequency response (knee frequency of 2,043 Hz) and an excellent long cycle stability. High specific capacitance of 596 F g⁻¹ indicates very high MnO₂ utilization owing to the much improved the electrical conductivity. In addition, the functional groups on CNTs ensure the strong bonding and excellent stability of the MnO₂ thin layer, revealed by the microscopic observations and electrochemical performance. The power density of 79 kW kg⁻¹ (with energy density of 6.2 Wh kg⁻¹ at current density of 100 A g⁻¹) shows its great potential to be used in high power applications, such as harbor lifting crane and laser power sources. The energy density of 70 Wh kg⁻¹ (with power density of 77.3W kg⁻¹ at current density of 0.1 A g⁻¹),

shows its high competitiveness compared with the current Ni-MH battery systems, thus makes it very promising to be implemented as the electric energy storage devices for hybrid vehicles. The facile synthesis of the SWNT/MnO₂ electrode is cost-efficient, easily controllable and highly scalable to be implemented in energy storage industry.

REFERENCES

- [1] C. Du, N. Pan, "*High power density supercapacitor electrodes of carbon nanotube films by electrophoretic deposition*" *Nanotechnology*, vol. 17, pp. 5314-5318, 2006.
- [2] C. Masarapu, H.F. Zeng, K.H. Hung, and B.Q. Wei, "*Effect of temperature on the capacitance of single-walled carbon nanotube supercapacitors*" *ACS Nano*, vol. 3, pp. 2199–2206, 2009.
- [3] K. S. Ryu, K. M. Kim, N. G. Park, Y. J. Park, S. H. Chang, "*Symmetric redox supercapacitor with conducting polyaniline electrodes*" *Journal of Power Sources*, vol.103, pp. 305-309, 2002.
- [4] J. H. Park, J. M. Ko, O.O. Park, D. W. Kim, "*Capacitance properties of graphite/polypyrrole composite electrode prepared by chemical polymerization of pyrrole on graphite fiber*", *Journal of Power Sources*, vol. 105, pp.20-25, 2002.
- [5] V. Subramanian, H. W. Zhu, R. Vajtai, P. M. Ajayan, B. Q. Wei, "*Hydrothermal synthesis and pseudocapacitance properties of MnO₂ nanostructures*" *Journal of Physical Chemistry B*, vol. 109, pp. 20207-20214, 2005.
- [6] H.L. Wang, H.S. Casalongue, Y.Y. Liang, H.J. Dai, "*Ni(OH)₂ nanoplates grown on graphene as advanced electrochemical pseudocapacitor materials*" *Journal of the American Chemical Society*, vol. 132, pp.7472-7477, 2010.
- [7] E. Frackowiak, V. Khomendo, K. Jurewicz, K. Lota, F. Beguin, "*Supercapacitors based on conducting polymers/nanotubes composites*" *Journal of Power Sources*, vol. 153, pp. 413-418, 2006.
- [8] I. H. Kim, J.H. Kim, B.W. Cho, Y.H. Lee, K.B. Kim, "*Synthesis and electrochemical characterization of vanadium oxide on carbon nanotube film substrate for pseudocapacitor applications*". *Journal of the electrochemical society*, vol. 153, pp. A989-A996, 2006.
- [9] S. W. Hwang, S. H. Hyun, "*Synthesis and characterization of tin oxide/carbon aerogel composite electrodes for electrochemical supercapacitors*" *Journal of Power Sources*, vol. 172, pp. 451-459, 2007.

- [10] T. Nathan, A. Aziz, A.F. Noor, S.R.S. Prabaharan, "Nanostructured NiO for electrochemical capacitors: synthesis and electrochemical properties", *Journal of Solid State Electrochemistry*, vol. 12, pp.1003-1009, 2008.
- [11] J. H. Park, O.O. Park, "Morphology and electrochemical behavior of ruthenium oxide thin film deposited on carbon paper", vol. 109, pp. 121-126, 2002.
- [12] X.J. Zhang, W. H. Shi, J.X. Zhu, D.J. Kharistal, W. Y. Zhao, B.S. Lalia, H.H. Hng, Q.Y. Yan, "High-Power and High-Energy-Density Flexible Pseudocapacitor Electrodes Made from Porous CuO Nanobelts and Single-Walled Carbon Nanotubes", *ACS Nano*, vol. 5, pp. 2013-2019, 2011.
- [13] R.L. Liang, H.Q. Cao, D. Qian, "MoO₃ nanowires as electrochemical pseudocapacitor materials", *Chemical Communications*, vol. 47, pp.10305-10307, 2011.
- [14] D. A. McKeown, P.L. Hagans, L. P. L. Carette, A. E. Russell, K. E. Swider, D. R. Rolison, "Structure of Hydrrous Ruthenium Oxides: Implications for Charge Storage", *The Journal of Physical Chemistry B*, vol.103, pp.4825-4832, 1999.
- [15] G.H. Yu, L. B. Hu, N. Liu, H. L. Wang, M. Vosgueritchian, Y. Yang, Y. Cui, Z. A. Bao, "Enhancing the supercapacitor performance of graphene/MnO₂ nanostructured electrodes by conductive wrapping" *Nano Letters*, vol. 11, pp.4438-4442, 2011.
- [16] E. Raymundo-Pinero, V. Khomenko, E. Frackowiak, F. Beguin, "Performance of manganese oxide/CNTs composites as electrode materials for electrochemical capacitors", *Journal of the Electrochemical Society*, vol. 152, pp. A229-A235, 2005.
- [17] Z. Fan, J. Chen, M. Wang, K. Cui, H. Zhou, Y. Kuang, "Preparation and characterization of manganese oxide/CNT composites as supercapacitive materials", *Diamond and Related Materials*, vol. 15, pp.1478-1483, 2006.
- [18] F. Teng, S. Santhanagopalan, D. D. Meng, *Solid State Science*, "Microstructure control of MnO₂/CNT hybrids under in-situ hydrothermal conditions", vol. 12, pp.1677-1682, 2010.
- [19] S. L. Chou, J. Z. Wang, S. Y. Chew, H. K. Liu, S. X. Dou, "Electrodeposition of MnO₂ nanowires on carbon nanotube paper as free-standing, flexible electrode for supercapacitors" *Electrochemistry Communications*, vol. 10, pp.1724-1727, 2008.

- [20] V. Subramanian, H. Zhu, B.Q. Wei, "Synthesis and electrochemical characterizations of amorphous manganese oxide and single walled carbon nanotube composites as supercapacitor electrode materials", *Electrochemical Communications*, vol. 8, pp. 827-832, 2006.
- [21] R. R. Jiang, T. Huang, Y. Tang, J. Liu, L. G. Xue, J. H. Zhuang, A. H. Yu, "Factors influencing MnO₂/multi-walled carbon nanotubes composite's electrochemical performance as supercapacitor electrode" *Electrochimica Acta*, vol. 54, pp. 7173-7179, 2009.
- [22] H. Zhu, B. Q. Wei, "Direct fabrication of single-walled carbon nanotube macro-films on flexible substrates", *Chemical Communications*, vol. 29, pp. 3042-3044, 2007.
- [23] V. Subramanian, H. Zhu, B.Q. Wei, "Nanostructured manganese oxides and their composites with carbon nanotubes as electrode materials for energy storage devices", *Pure and Applied Chemistry*, vol. 80, pp. 2327-2343, 2008.
- [24] V. Subramanian, H. Zhu, B.Q. Wei, "Alcohol-assisted room temperature synthesis of different nanostructured manganese oxides and their pseudocapacitance properties in neutral electrolyte", *Chemical Physics Letters*, vol. 453, pp. 242-249, 2008.
- [25] M. Ue, K. Ida, S. Mori, "Electrochemical properties of organic liquid electrolytes based on quaternary onium salts for electrical double-layer capacitors", *Journal of the Electrochemical Society*, vol. 141, pp. 2989-2995, 1994.
- [26] S. B. Ma, K. Y. Ahn, E. S. Lee, K. H. Oh, K. B. Kim, "Synthesis and characterization of manganese dioxide spontaneously coated on carbon nanotubes" *Carbon*, vol. 25, pp. 375-382, 2007.
- [27] H. Q. Wang, Z. S. Li, J. H. Yang, Q. Y. Li, X. X. Zhong, "A novel activated mesocarbon microbead(aMCMB)/Mn₃O₄ composite for electrochemical capacitors in organic electrolyte" *Journal of Power Sources*, vol. 194, pp. 1218-1221, 2009.
- [28] P. Simon, Y. Gogotsi, "Materials for Electrochemical Capacitors", *Nature Materials*, vol. 7, pp. 845-854, 2008.
- [29] C. Masarapu, H. F. Zeng, K. H. Hung, B. Q. Wei, "Effect of temperature on the capacitance of carbon nanotube supercapacitors", *ACS Nano*, vol. 3, pp. 2199-2206, 2009.

- [30] M. Hughes, G. Z. Chen, M. S. P. Shaffer, D. J. Fray, A. H. Windle, "*Electrochemical capacitance of a nanoporous composite of carbon nanotubes and polypyrrole*" *Chemistry of Materials*, vol. 14, pp. 1610-1613, 2002.
- [31] P. C. Chen, H. T. Chen, J. Qiu, C. W. Zhou, "*Inkjet printing of single-walled carbon nanotube/RuO₂ nanowire supercapacitors on cloth fabrics and flexible substrates*", *Nano Research*, vol. 3, pp.594-603, 2010.
- [32] C. G. Liu, M. Liu, F. Li, H. M. Cheng, "*Frequency response characteristic of single-walled carbon nanotubes as supercapacitor electrode material*", *Applied Physics Letters*, vol. 92, pp. 143108, 2008.
- [33] C. S. Du, N. Pan, "*Supercapacitors using carbon nanotubes films by electrophoretic deposition*", *Journal of Power Sources*, vol. 160, pp. 1487-1494, 2006.
- [34] Z. Fan, J. Yan, T. Wei, L. Zhi, G. Ning, T. Li, F. Wei, "*Asymmetric supercapacitors based on graphene/MnO₂ and activated carbon nanofiber electrodes with high power and energy density*" *Advanced Functional Materials*, vol. 21, pp. 2366-2375, 2011.
- [35] F. Ataherian, N.L. Wu, "*Long-term charge/discharge cycling stability of MnO₂ aqueous supercapacitor under positive polarization*", *Journal of the Electrochemical Society*, vol. 158, pp. A422-A427, 2011.

Chapter 5 CONCLUSIONS, PUBLICATIONS AND FUTURE WORK

5.1 Conclusions

Compressive pressure effect of the SWNT electrode supercapacitor, the dynamic stretchable supercapacitor, and the facile and super capacitive behavior of the SWNT/MnO₂ hybrid films, are demonstrated in this thesis. In chapter 2, the electrochemical behaviors of the SWNT electrode and various aqueous electrolyte-based supercapacitors are systematically studied, which shows the improved wetting and electrode/electrolyte interface under the pressure. In Chapter 3, with the successful development of the elastomeric separator and the implementation with the previously developed the stretchable SWNT electrode, the dynamic stretchable supercapacitor prototype was achieved. The process is facile, scalable and cost-efficient. The cells obtain excellent cycling stability, with extremely high strain rate of 4.46% strain s⁻¹, and high reversible strain of 31.5%. The dynamic electrochemical behavior of the cell during the *In situ* stretching and releasing is discovered. In Chapter 4, a facile, scalable and cost-efficient method to fabricate SWNT/MnO₂ supercapacitor was introduced and investigated, which significantly improves the energy density of the supercapacitor, as well as keeping excellent power density and cycling stability of the whole device.

5.2 Publications

- [1] X. Li, J.P. Rong, B.Q. Wei, "Electrochemical Behavior of Single-Walled Carbon Nanotube Supercapacitors under Compressive Stress" ACS Nano, vol. 4, pp 6039–6049, 2010.
- [2] X. Li, B.Q. Wei, "Facile synthesis and super capacitive behavior of SWNT/MnO₂ hybrid films", Nano Energy, vol. 1, pp 479–487.
- [3] Y. An, X. Li, B. Q. Wei, and H. Jiang, "A statistical mechanics model of carbon nanotube macro-films" Theoretical & Applied Mechanics Letters, 1, 041003, 2011.
- [4] C. Yu, X. Li, T. Ma, J.P. Rong, R.J. Zhang, J. Shaffer, Y. An, Q. Liu, B.Q. Wei, "Silicon Thin Films as Anodes for High-Performance Lithium-Ion Batteries with Effective Stress Relaxation" Advanced Energy Materials, vol. 2, pp.68–73, 2012.
- [5] C. Masarapu, L.P. Wang, X. Li, B.Q. Wei, "Tailoring Electrode/Electrolyte Interfacial Properties in Flexible Supercapacitors by Applying Pressure" Advanced Energy Materials, vol. 2, pp 546-552.

5.3 Future Work

Although SWNT macro-films and SWNT/MnO₂ hybrid films based supercapacitor showed promising applications in improving power density, energy density and cycling stability, there is still a great progress need to done to simplify the fabrication process, to increase the electrode mass load in the limited volume, and to make it applicable in commercial products.

One limitation of dynamic stretchable supercapacitor developed at this stage, is that it is still have relatively low volumetric specific capacitance, due to the relatively thick package materials need to ensure the mechanical robustness. The rigid copper collector inside the cell would be suggested to be replaced with stretchable interconnects, such as buckled gold layer. The sealing issue of the whole device and the energy density would still need to be improved in the future work. It is suggested to explore the fully stretchable lithium-ion battery system with the elastomeric electrospun separator, to fulfill the energy requirement of the future stretchable electronic devices.

Another limitation of the current pre-strained made stretchable electrode is that the stretching direction is limited to the direction previous set up by the stretching. It is possible to make multidirectional, elastomeric, compressible, stretchable energy storage device by synthesize the elastomeric electrospun membrane first to provide mechanical backbone, then coated with the conductive polymer and active electrode materials to further improve the performance of the cell.